POLITECNICO DI TORINO
Repository ISTITUZIONALE

Data-driven turbulent heat flux modeling with inputs of multiple fidelity

Original
Data-driven turbulent heat flux modeling with inputs of multiple fidelity / Fiore, M., Saccaggi, E., Koloszar, L., Bartosiewicz, Y., Mendez, M.A.. - In: PHYSICAL REVIEW FLUIDS. - ISSN 2469-990X. - 10:(2025). [10.1103/PhysRevFluids.10.034606]

Availability:
This version is available at: 11583/2998342 since: 2025-12-03T13:22:37Z

Publisher:
APS

Published
DOI:10.1103/PhysRevFluids.10.034606

Terms of use:

This article is made available under terms and conditions as specified in the corresponding bibliographic description in the repository

Publisher copyright
APS postprint/Author's Accepted Manuscript e postprint versione editoriale/Version of Record

(Article begins on next page)

23 November 2026

Data-driven turbulent heat flux modeling with inputs of multiple fidelity

Matilde Fiore,[1,*] Enrico Saccaggi,[2,1] Lilla Koloszar,[1] Yann Bartosiewicz,[3] and Miguel A. Mendez[1]

[1]*Environmental and Applied Fluid Dynamics Department, von Karman Institute for Fluid Dynamics, Belgium*
[2]*Department of Mechanical and Aerospace Engineering, Politecnico di Torino, Italy*
[3]*Institute of Mechanics, Materials and Civil Engineering (IMMC), Universite catholique de Louvain (UCLouvain), Place du Levant 2, 1348 Louvain-la-Neuve, Belgium*

(Dated: December 3, 2025)

Data-driven RANS modeling is emerging as a promising methodology to exploit the information provided by high-fidelity data. However, its widespread application is limited by challenges in generalization and robustness to inconsistencies between input data of varying fidelity levels. This is especially true for thermal turbulent closures, which inherently depend on momentum statistics provided by low or high fidelity turbulence momentum models. This work investigates the impact of momentum modeling inconsistencies on a data-driven thermal closure trained with a dataset with multiple fidelity (DNS and RANS). The analysis of the model inputs shows that the two fidelity levels correspond to separate regions in the input space. It is here demonstrated that such separation can be exploited by training with heterogeneous data, allowing the model to detect the level of fidelity in its inputs and adjust its prediction accordingly. In particular, sensitivity analysis and verification show that such a model can leverage data inconsistencies to increase its robustness. Finally, the verification with a CFD simulation shows the potential of this multi-fidelity training approach for flows in which momentum statistics provided by traditional models are affected by model uncertainties.

I. INTRODUCTION

Data-driven methods are progressively entering the field of turbulence modeling as one of the most promising avenues to overcome the modeling barrier reached by traditional approaches in the last decade. A variety of data-driven approaches for the modeling of Reynolds stresses have been recently proposed [1–5], among which artificial neural networks [1, 5–8] are widely adopted to handle large databases and provide complex, non-linear input/output mappings. Despite the merits of these approaches, significant limitations still restrict their use for a wide range of CFD (Computational Fluid Dynamics) simulations.

Zhang *et al.* [9] highlights the most important of these limitations, including the lack of generality in data-driven closures, i.e., their limited applicability to flows that deviate from the conditions covered by the training. The derived closures usually target specific classes of flows [10–12]. The existence of general or universal data-driven turbulence models is currently being questioned by the community [13] due to the yet unclear impact of turbulent coherent structures on geometry, Reynolds number, and many other local/global conditions. Moreover, the literature points out limitations when data-driven closures are trained offline [14], i.e., with high-fidelity data only in a *frozen* mode. This training strategy neglects the influence of the numerical methods and additional sub-models involved in the CFD setup. The frozen training mode causes model-data inconsistencies [14], where the quantities taken as input by the model differ during training and testing phases. This limits the accuracy when the model is applied a posteriori. A typical example of the consistency problem is the turbulent time scale k/ε, which is systematically different in the high-fidelity and modeled RANS (Reynolds Averaged Navier-Stokes) data, leading to inconsistencies in the data-driven closure if this quantity is one of the inputs of the model [15].

This work proposes mitigating this issue by partially replacing the critical high-fidelity turbulent statistics with their RANS counterparts. This approach is followed, for example, by Schmelzer *et al.* [15], who developed a k-corrective frozen training strategy where the turbulent dissipation rate ε is computed by solving its RANS transport equation, taking all the other statistics from the high-fidelity database and adding a corrective term accounting for errors in the k production term. Weatheritt and Sandberg [16] proposed a similar approach in which $\omega = \varepsilon/k$ is computed from RANS equations evaluated with high-fidelity mean flow and Reynolds stresses. Yin *et al.* [3] included the inconsistency between the RANS and the Direct Numerical Simulation (DNS) estimates of k in the output of the data-driven model and used this to inform the data-driven model when it operates in conjunction with and RANS solver.

Addressing model inconsistencies in turbulence modeling generally requires balancing the physical consistency of the data-driven model with its applicability in standard RANS solvers. On the one hand, employing modeled statistics enhances the practicality of the closures but inevitably introduces structural errors in the mapping to offset input inaccuracies. On the other hand, leveraging high-fidelity data improves physical consistency and captures the true correlations among the statistics, but this comes at the cost of reduced applicability when integrated into RANS solvers. Moving to non-isothermal problems, turbulent heat flux modeling depends on momentum turbulence modeling, and the Reynolds stress tensor is inevitably one of the critical inputs for turbulent heat flux models. Consequently, a thermal turbulence model trained with Reynolds stresses derived from high-fidelity data makes significant errors when deployed in a RANS solver, which uses low-fidelity modeling of Reynolds stresses along with the Boussinesq approximation.

* matilde.fiore@vki.ac.be

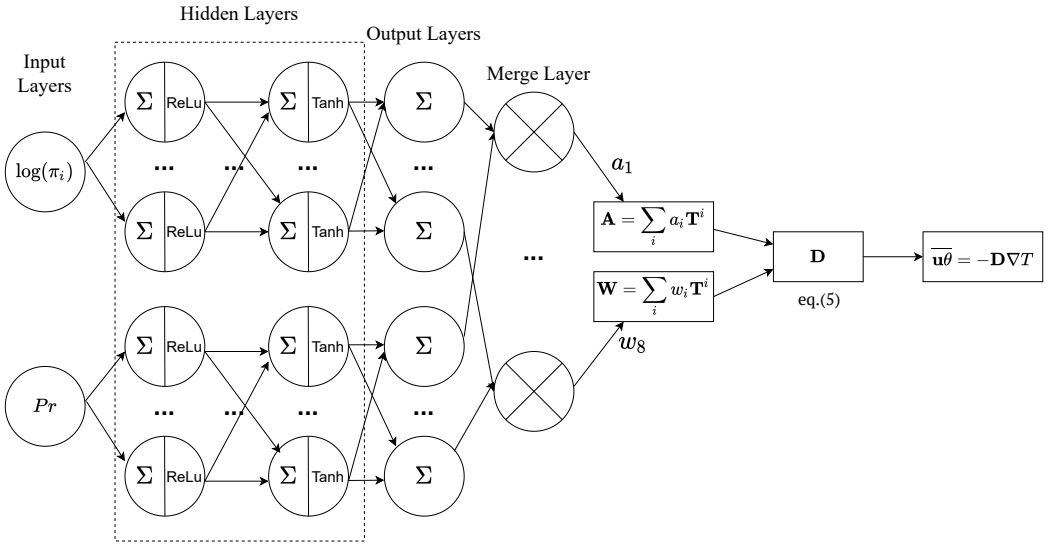

FIG. 1: Structure of the artificial neural network used to predict the turbulent heat flux as a function of the molecular Prandtl number and the basis of invariants indicated in Table I. Figure reproduced from [17].

This problem was highlighted in [18], focusing on the data-driven modeling of the turbulent heat flux at near unity and low Prandtl numbers. Model inconsistencies in the Reynolds stresses were identified to be the major challenge in data-driven thermal closures, partially addressable only by the use of second-order momentum turbulence closures. Modeling the Reynolds stresses with the eddy viscosity concept poses significant limitations to thermal turbulence modeling because the turbulence anisotropy is essential to represent the heat flux vector and is indeed the foundation of most algebraic thermal closures [19–21]. Such modeling choices are typical of both data-driven and theory-driven RANS modeling. In fact, traditional thermal models are often developed to be combined with specific momentum closures [22, 23], or variants are proposed to account for different momentum models [24].

This work explores the hypothesis that machine learning tools could identify the source of the input (e.g., high fidelity vs low fidelity momentum modeling) and adapt accordingly or find compromises by mitigating its sensitivities to critical inputs. Both approaches could ensure an optimal compromise between the physical consistency of the model when it is deployed on high-fidelity data and robustness when it is deployed with traditional RANS solvers.

To explore this hypothesis, this paper proposes a training method based on inputs of multiple-fidelity multi-objective optimization. More specifically, the training of a data-driven model for the turbulent heat flux, introduced in section II, was carried out with a *hybrid* dataset consisting of high-fidelity (DNS) and low fidelity (RANS) data. The peculiarities of such heterogeneous dataset are discussed in section III. The learning performances are analyzed in section IV: from the model choices within the input space to the verification of the learned closure and its sensitivity analysis. The validation of the model is primarily aimed at estimating the robustness gain obtained with this strategy. Based on the results presented in section V, conclusions and future development are presented in section VI.

II. DATA-DRIVEN AHFM

The data-driven Algebraic Heat Flux Model (AHFM) considered in this work is a physics-constrained Artificial Neural Network (ANN) that predicts the turbulent heat flux at near unity and low Prandtl numbers. Details of its architecture are provided in [17, 18] and briefly recalled in this section for completeness.

The network embeds rotational invariance properties by construction, as proposed by Ling *et al.* [1], and its predictions are realizable, i.e. they satisfy the second law of thermodynamics. Figure 1 provides a schematic of the neural network structure and its layers. Specifically, the network consists of two input layers, one for the whole set of invariants listed in Table 1 and the second for the Prandtl number only. The choice of two separate input layers led to good training performance, probably due to the limited interdependency between the Prandtl number and the remaining invariants. The network predicts variable closure coefficients a_i and w_i based on a set of dimensionless invariants, denoted as π_i and defined on the left column of Table I. Among the quantities listed in the table, k represents the turbulent kinetic energy, ε the turbulent dissipation rate, k_θ the variance of the thermal fluctuations, and ε_θ the thermal turbulent dissipation rate. The quantities ν and α_l denote the molecular viscosity and diffusivity, respectively, while the tensors $\mathbf{S}$, $\mathbf{\Omega}$ and $\mathbf{b}$ are defined as:

$$\mathbf{S} = \frac{1}{2}\left(\frac{\partial \mathbf{U}}{\partial \mathbf{x}} + \frac{\partial \mathbf{U}}{\partial \mathbf{x}}^T\right), \tag{1}$$

$$\mathbf{\Omega} = \frac{1}{2}\left(\frac{\partial \mathbf{U}}{\partial \mathbf{x}} - \frac{\partial \mathbf{U}}{\partial \mathbf{x}}^T\right), \tag{2}$$

$$\mathbf{b} = \frac{\overline{\mathbf{uu}}}{k} - \frac{2}{3}\mathbf{I}, \tag{3}$$

in which $\mathbf{U}$ is the mean velocity field, $\mathbf{u}$ the velocity fluctuation and the operator $\bar{\cdot}$ denotes the Reynolds averaging. Tensor $\mathbf{b}_2$ involved in the definition of π_5 denotes the projection of $\mathbf{b}$ on the main $(x-y)$ plane of the flow, i.e.

$$\mathbf{b}_2 = \begin{pmatrix} b_{11} & b_{12} & 0 \\ b_{12} & b_{22} & 0 \\ 0 & 0 & 0 \end{pmatrix}. \tag{4}$$

The coefficients a_i and w_i are used to compute the following expansions of tensors:

$$\mathbf{A} = \sum_{i=1}^{n} a_i \mathbf{T}^i, \qquad \mathbf{W} = \sum_{i=1}^{n} w_i \mathbf{T}^i, \tag{5}$$

in which $\mathbf{T}^i$ are the element of the tensor basis indicated in Table I. The dispersion tensor is then computed as a sum of a symmetric, positive-definite tensor and a skew-symmetric tensor:

$$\mathbf{D} = \left[(\mathbf{A} + \mathbf{A}^T)(\mathbf{A}^T + \mathbf{A}) + \frac{k}{\varepsilon^{0.5}}(\mathbf{W} - \mathbf{W}^T) \right], \tag{6}$$

In Ref. [17, 18], the network was trained with high-fidelity DNS data for Prandtl numbers ranging from 0.71 to 0.01. The loss function applied for the training promotes the smoothness of the predicted heat flux fields:

$$\begin{aligned} \mathscr{L}(\mathbf{q}) = \frac{1}{N}\left(\sum_{i=1}^{N} \sum_{j=1}^{3} \left(\hat{q}_{i,j} - q_{i,j} \right)^2 \right) \\ + \frac{\lambda}{N}\left(\sum_{i=1}^{N} \sum_{j,k=1}^{3} \left| \frac{\partial \hat{q}_{i,j}}{\partial x_k} - \frac{\partial q_{i,j}}{\partial x_k} \right| \Delta x_k \right), \end{aligned} \tag{7}$$

where $i \in [1, \ldots N]$ is the index spanning across the N data points contained in each mini-batch, $q_{i,j} = \overline{u_j \theta}$ is the prediction of the ANN and $\hat{q}_{i,j}$ is the corresponding flux provided by DNS data. Both values $q_{i,j}$ and $\hat{q}_{i,j}$ are normalized with respect to the maximum DNS value achieved in each flow configuration.

Once trained, the data-driven AHFM was verified with non-isothermal simulations run in OpenFoam, for which the model was compared with other theory-driven closures [22, 24, 25]. The verification highlighted the sensitivity of the data-driven AHFM to the momentum turbulence model applied in combination with it. As an example, Figure 2 presents the validation of the data-driven AHFM (denoted as ANN in the Figure) for turbulent channel flow, and the comparison with other theory-driven models such as the Manservisi model (MM) [22], the Kays correlation [25] and the AHFM developed by Shams (AHFM) [24]. In the figures on the left, the AHFM is coupled with the Elliptic Blending Reynolds Stress Model (EBRSM) [26] while in the figure on the right, the AHFM is coupled with the Launder-Sharma k-ε. Note that when the Reynolds stresses are accurately modeled with second-order closures, the data-driven AHFM outperforms the traditional AHFM considered for comparison [22, 24, 25]. However, the accuracy deteriorates when the network receives Reynolds stresses modelled with the Linear Eddy Visocisty Model (LEVM), because of its dependency on the Reynolds stress anisotropy $\mathbf{b}$, defined by eq. (3).

Hence, the comparison shown in Figure 2 highlights that the data-driven AHFM cannot handle deficiencies of momentum modeling. This is a significant limitation of the machine learning closure, which restricts its applicability in CFD solvers.

Invariant Basis	Tensor Basis
$\pi_1 = \frac{k^2}{\varepsilon^2}\{\mathbf{S}^2\}$, $\pi_2 = \frac{k^2}{\varepsilon^2}\{\mathbf{\Omega}^2\}$,	$\mathbf{T_1} = \frac{k}{\varepsilon^{0.5}}\mathbf{I}$, $\mathbf{T_2} = \frac{k}{\varepsilon^{0.5}}\mathbf{b}$,
$\pi_3 = \frac{1}{\{\mathbf{b}^2\}}$, $\pi_4 = \frac{k}{\varepsilon}\{\mathbf{bS}\}$,	$\mathbf{T_3} = \frac{k^2}{\varepsilon^{1.5}}\mathbf{S}$, $\mathbf{T_4} = \frac{k^2}{\varepsilon^{1.5}}\mathbf{\Omega}$,
$\pi_5 = \{\mathbf{b_2}\}$, $\pi_6 = \frac{k^2}{\varepsilon^2}\{\mathbf{bS\Omega}\}$,	$\mathbf{T_5} = \frac{k^2}{\varepsilon^{1.5}}\mathbf{bS}$, $\mathbf{T_6} = \frac{k^2}{\varepsilon^{1.5}}\mathbf{b\Omega}$,
$\pi_7 = \frac{\|\nabla\theta\|}{\sqrt{k_\theta}}\frac{k^{1.5}}{\varepsilon}$, $\pi_8 = \frac{k_\theta \varepsilon}{k \varepsilon_\theta}$	$\mathbf{T_7} = \frac{k^3}{\varepsilon^{2.5}}\mathbf{S\Omega}$,
$Re_t = \frac{k^2}{\varepsilon \nu}$, $Pr = \frac{\nu}{\alpha_t}$,	$\mathbf{T_8} = \frac{k^2}{\varepsilon^{2.5}}\mathbf{bS\Omega}$,

TABLE I: Formulation of the invariant and tensor basis, computed according to [18]. The operator $\{\cdot\}$ denotes the tensor trace. The reader is referred to the nomenclature and to Ref.[18] for the detailed definition of the symbols.

III. MULTI-FIDELITY DATABASE AND PRELIMINARY ANALYSES

The database employed to train the data-driven AHFM consists of high-fidelity (DNS) data for non-isothermal turbulent channel flow [27, 28] and non-isothermal backward-facing step [29] at various Reynolds and Prandtl numbers. An additional dataset of a non-isothermal planar impinging jet [30] was employed for testing. The details about the reference DNS data are provided in Table II. The training database is extended in the present work with RANS counterparts of the same flows simulated in the OpenFoam environment [31]. For the RANS simulations, the Launder-Sharma k-ε model was selected as the turbulence model. The computational domains were discretized to achieve y^+ ranging from 0.1 to 1.0. The RANS simulations were limited to the momentum field, i.e. the temperature field was not resolved. The reader is referred to Appendix B for further details about the computational setup for the training data.

The DNS and RANS data collected were manipulated to calculate the tensors $\mathbf{T}^i$ and invariants π_i indicated in Table I. For turbulent channel flow, the discrepancy between the π_i calculated with the two data sets is shown in Figure 3, which represents the invariants in their 10-dimensional space with red (DNS) and green (RANS) lines. Specifically, each line in the plot indicates the values of the input features at each point of the computational mesh. Only 500 of 425400 points that comprise the training database are depicted for visualization purposes.

TABLE II: Available DNS databases for forced convection at different *Re* and *Pr* numbers

Author and Ref.	Flow Configuration	Reynolds number*	Prandtl number	Usage
Kawamura et al.[27]	Channel flow	Re_τ=180-640	0.025-0.71	training/test
Tiselj et al. [28]	Channel flow	Re_τ=180-590	0.01	training/test
Oder et al. [29]	Backward-Facing Step	Re_b=3200	0.1,0.005	training/test
Duponcheel et al. [32]	Impinging jet Flow	Re_τ =550	0.031	test

* The complete definition of the Reynolds number for each flow configuration can be found in the related references.

As expected, the distribution of the invariants π_1 and π_2, π_7 and π_8 and Re_t is similar between RANS and DNS since these only involve isotropic turbulent quantities and the derivatives of the mean fields ($\mathbf{U}$ and T). On the other hand, significant differences appear in the invariants related to the anisotropic part of the Reynolds stress tensor $\mathbf{b}$, that is, π_3, π_4, π_5, and π_6. In fact, this behavior of the invariants reflects the differences in the tensor $\mathbf{b}$ that can be seen in Figure 4, which depicts the Reynolds stress anisotropy in the barycentric map [33] for the two data sets in case of turbulent channel flow.

This representation shows that the maximum distance between the turbulent states predicted by the two approaches occurs at $y^+ < 30$, where the anisotropy is severely misrepresented. The gap decreases at higher y^+, for which the points move towards the state of pure isotropy.

IV. METHODOLOGY

The proposed methodology for a model handling heterogeneous input data combines dimensionality reduction, multiobjective optimization, sensitivity analysis, and uncertainty quantification. We describe the various steps in the following. Concerning the dimensionality reduction, Principal Component Analysis (PCA) was used to identify the optimal combination of features describing the different levels of fidelity as described in Section IV A. Section IV B reports on multiobjective optimization at the foundation of model training. The performances of the model obtained with this training are analyzed and compared with the original data-driven AHFM by inspecting its output layer and estimating its sensitivities in terms of Shapley values, introduced in section V C. Finally, the data-driven model is implemented in a CFD solver (OpenFoam), and there tested for a non-isothermal planar impinging jet at $Pr = 0.01$. The details of this validation test case and the simulation setup are provided in section IV E.

A. Principal Component Analysis (PCA)

The PCA was applied on the feature matrix $\mathbf{X} \in \mathbb{R}^{N\times F}$, collecting the value of all the F features on the N grid points of both the training datasets. The reader is referred to [34] for an introduction to the PCA.

The goal was to identify $P < F$ linear combinations of the input features F that explain most of the input variance and hence restrict the dimensionality of the input of the model along the associated principal directions, here denoted as $\mathbf{v}_i$, with $i = [1,..P]$. These directions are eigenvectors of the covariance matrix $\mathbf{S}$

$$\mathbf{S} = \frac{1}{N-1}(\mathbf{X}-\mathbf{x}_\mu)^T(\mathbf{X}-\mathbf{x}_\mu), \tag{8}$$

where $\mathbf{x}_\mu \in \mathbb{R}^N$ is the vector containing the average of each column. Denoting as $\mathbf{V} = [\mathbf{v}_1 \dots \mathbf{v}_P] \in \mathbb{R}^{N\times P}$ the matrix collecting the leading P eigenvectors and $\mathbf{\Lambda} \in \mathbb{R}^{P\times P}$ the diagonal matrix with the associated eigenvalues sorted in decreasing order, the reduced feature space can be written as $\tilde{\mathbf{X}} = \mathbf{X}\mathbf{V} \in \mathbb{R}^{N\times P}$.

The correlations between the original variable and the principal components can be evaluated from the load matrix $\mathbf{L} = \mathrm{Cov}(\mathbf{X}, \tilde{\mathbf{X}}) \in \mathbb{R}^{F\times P}$. Introducing the Singular Value Decomposition of the feature matrix $\mathbf{X} = \mathbf{U}\sqrt{\mathbf{\Lambda}}\mathbf{V}^T$, the load matrix can be computed as defined as

$$\mathbf{L} = \mathrm{Cov}(\mathbf{X}, \tilde{\mathbf{X}}) = \frac{\mathbf{X}^T\tilde{\mathbf{X}}}{N-1} = \frac{\mathbf{V}\sqrt{\mathbf{\Lambda}}\mathbf{U}^T\mathbf{U}\sqrt{\Lambda}}{N-1} = \frac{\mathbf{V}\mathbf{\Lambda}}{N-1}. \tag{9}$$

B. Multi-fidelity training

We denote as $\mathbf{X}_{lf}$ the feature matrix collecting data from low-fidelity simulations and as $\mathbf{X}_{hf}$ the one collecting data from high-fidelity simulations. To ensure reasonable predictions with both sets of data, the artificial neural network must be trained on the inconsistencies of the input data between the two fidelity levels. Denoting with $\mathbf{y}_{lf}$ and $\mathbf{y}_{hf}$ the predictions of the model with the inputs $\mathbf{X}_{lf}$ and $\mathbf{X}_{hf}$, and with $\hat{\mathbf{y}}_{hf}$ the reference values provided by the high-fidelity database, the cost function driving the training in case of multi-fidelity inputs is taken as:

$$\mathscr{L} = \mathscr{L}(\mathbf{y}_{hf}, \hat{\mathbf{y}}_{hf}) + \alpha\mathscr{L}(\mathbf{y}_{lf}, \hat{\mathbf{y}}_{hf}), \tag{10}$$

in which $\mathscr{L}(\cdot)$ is defined by (7). This choice of the loss translates the previous regression problem introduced in section II

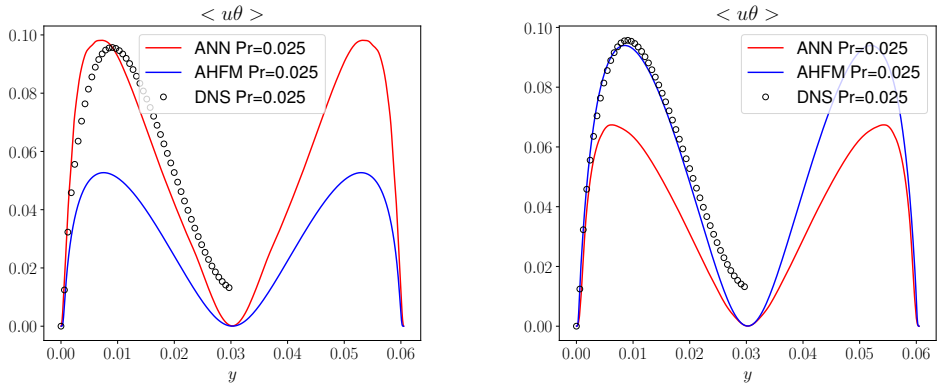

(a) $\overline{u\theta}$

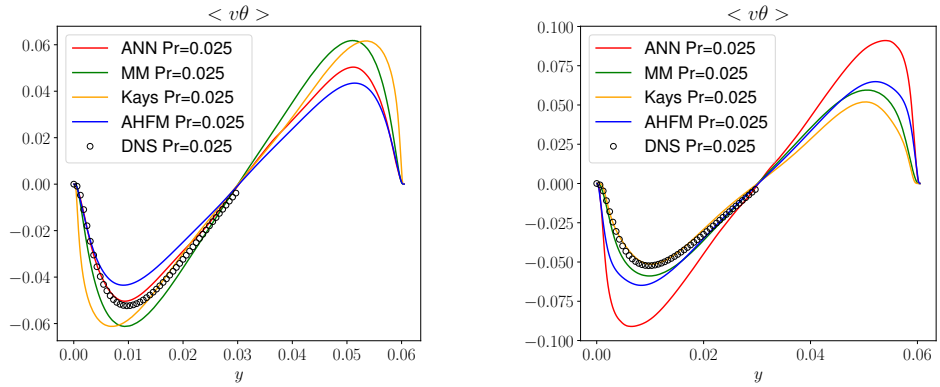

(b) $\overline{v\theta}$

FIG. 2: Comparison of the results achieved with the data-driven model (ML), the Manservisi model (MM), the Kays correlation, and the AHFM model at Re_τ=395 and Pr=0.025 as thermal turbulence models, and the EBM (left) and the Launder-Sharma k-ε (right) as momentum turbulence models.

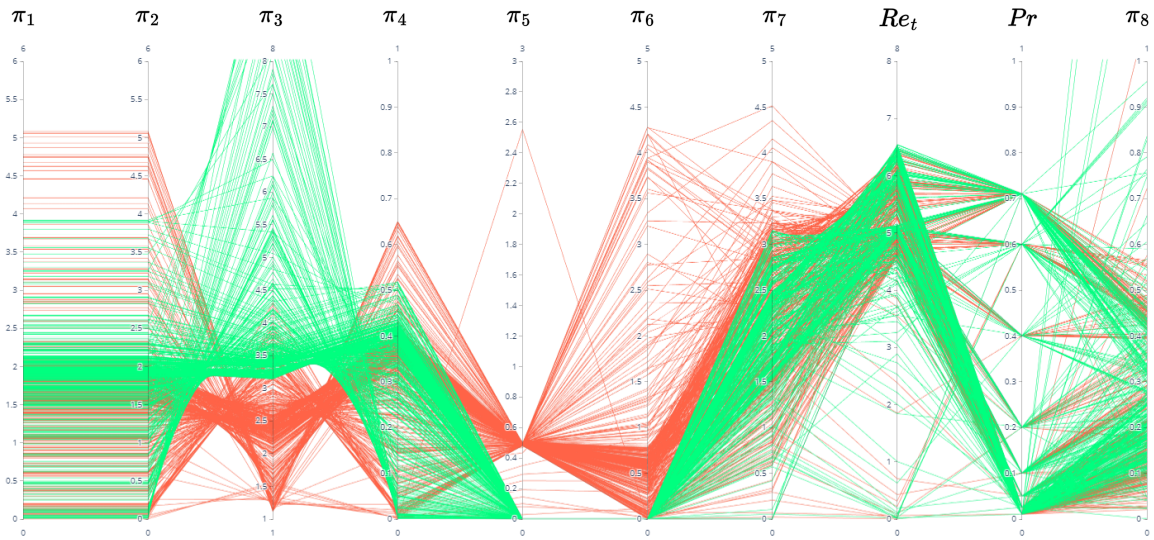

FIG. 3: Visualization of the DNS (red) and RANS (green) inputs in their 10-dimensional space for non-isothermal turbulent channel flow ($Re_\tau = 640$, $Pr = 0.025$).

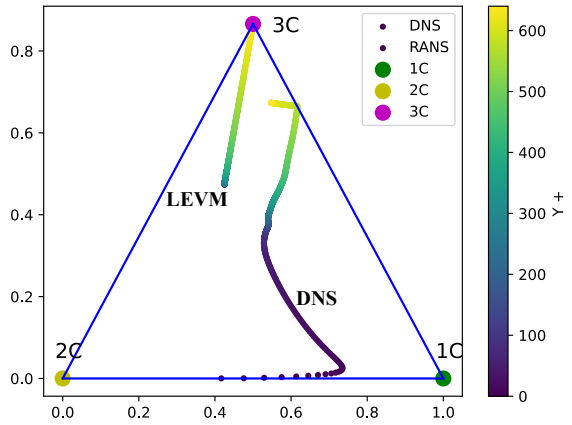

FIG. 4: Anisotropic turbulence visualisation in a barycentric map in case of a turbulent channel flow. The distance between the DNS state and the Linear Eddy Viscosity Model (LEVM) can be highlighted.

into a multi-objective optimization problem in which the errors computed with both families of inputs need to be minimized. The scalar α in (10) varies between 0.001 and 1000 to build the Pareto front of the multi-objective problem.

C. Shapley values

We analyze the model sensitivity to its features using Shapley values [35]. Shapley values, originating from cooperative game theory, offer a way to distribute the total gain (or cost) among the players (or features) based on their marginal contributions. For a model f with input features $\mathbf{X} = (\mathbf{x}_1, \mathbf{x}_2, \ldots, \mathbf{x}_F)$, the Shapley value ϕ_i for the feature $\mathbf{x}_i$ is defined as:

$$\phi_i = \sum_{S \subseteq K \setminus \{i\}} \frac{|S|!(|K| - |S| - 1)!}{|K|!} \left[f(S \cup \{i\}) - f(S) \right], \quad (11)$$

in which K is the set including all F features, S is a subset of N features not containing X_i, $|S|$ is the cardinality of subset S, and $f(S)$ denotes the model prediction using the subset of features S. The term $f(S \cup \{i\}) - f(S)$ represents the marginal contribution of feature $\mathbf{x}_i$ when added to the subset S. The Shapley value calculation involves averaging these marginal contributions on all possible subsets S, weighted by the combinatorial factors $|S|!(|K| - |S| - 1)!/|K|!$. Note that, compared to other approaches for sensitivity analysis (e.g. the Integrated Gradient method [36] applied in [18]) this method provides more complete information about the sensitivity of the model, since the discrepancies in eq. (11) is evaluated over the whole input space instead of targeting specific trajectories. Specifically, the predictions $f(S)$ for each subset are computed by averaging the model evaluations obtained by perturbing the features excluded from the subset S around their predefined baseline values. In the present case, the baseline values of the ablated features is considered their average over the entire range of flows considered in the database indicated in Table II.

Note that based on eq. (11) the computational cost of the Shapley method is given by the product of the number of features with their number of permutations, i.e., $F \cdot F!$, which would lead to $18 \cdot 18!$ model evaluations based on the list of features reported in Table I. To reduce the computational cost, the features were assigned to four main groups that will also facilitate the interpretation of the results. These groups, reported in Table III, are:

- Group 1: Momentum isotropic features (MI) depending on the velocity gradient and isotropic momentum statistics (e.g. k, ε);
- Group 2: Momentum anisotropic features (MA) depending on the anisotropic part of the Reynolds stress tensor $\mathbf{b}$;
- Group 3: Thermal-based features (TH) depending on the molecular Prandtl number and thermal related statistics;
- Group 4: The basis tensors (TE) indicated in Table I.

D. Uncertainty propagation

The uncertainty analysis of the trained data-driven AHFMs was carried out to evaluate their robustness with respect to the momentum treatment. The method is based on the perturbation of the turbulent state in the barycentric map shown in Figure 4 and, specifically, between the true state (DNS) and the one predicted by Linear Eddy Viscosity Models (LEVMs). The coordinates of the points on the map are computed from the eigenvalues ψ_i ($i = 1,2,3$) of the anisotropic part of the Reynolds stress tensor $\mathbf{b}$. The vertices of the triangle ($\mathbf{z}_{1C}$,$\mathbf{z}_{2C}$,$\mathbf{z}_{3C}$) represent the limiting states of turbulence:

- one component ($\mathbf{z}_{1C} = [1,0]$) for which $\psi_i = \frac{2}{3}, -\frac{1}{3}, -\frac{1}{3}$.
- two components ($\mathbf{z}_{2C} = [0,0]$) for which $\psi_i = \frac{1}{6}, -\frac{1}{6}, -\frac{1}{3}$.
- isotropic ($\mathbf{z}_{3C} = [1/2, \sqrt{3}/2]$), for which ψ_i are all zero.

Each point $\mathbf{z} \in \mathbb{R}^2$ in this plane is associated to a specific set of eigenvalues $\psi \in \mathbb{R}^3$ by a linear mapping [33]:

$$\mathbf{z}^* = \mathbf{z}_{1C}(\psi_1 - \psi_2) + \mathbf{z}_{2C}(2\psi_2 - 2\psi_3) + \mathbf{z}_{3C}(3\psi_3 + 1), \quad (12)$$

complemented with the conditions:

$$\psi_1 + \psi_2 + \psi_3 = 0. \quad (13)$$

Writing the mapping $\psi \to \mathbf{z}$ as $\mathbf{z} = \mathbf{B}\psi$, its inverse becomes $\psi = \mathbf{B}^{-1}\mathbf{z}$.

This mapping was here used to propagate uncertainties in the baricentric map to uncertainties in the associated anisotropic stresses and then the turbulent heat flux through

TABLE III: Features grouped for the Shapley value analysis. The definition of the features can be found in Table I.

Groups of features for the Shapley value analysis			
Momentum isotropic (MI)	**Thermal (TH)**	**Momentum anisotropic (MA)**	**Tensors (TE)**
π_1, π_2	Pr, π_8	π_5, π_3	$\mathbf{T}_1$, $\mathbf{T}_2$, $\mathbf{T}_3$, $\mathbf{T}_4$
π_4, Re_τ	π_7, ∇T	π_6	$\mathbf{T}_5$, $\mathbf{T}_6$, $\mathbf{T}_7$, $\mathbf{T}_8$

the model. To this end, the high-fidelity (DNS) state $\mathbf{z}_{hf}$ in the barycentric map is perturbed towards the state of turbulence given by the low fidelity (RANS) momentum treatment $\mathbf{z}_{lf}$, leading to a modified location $\mathbf{z}^*$:

$$\mathbf{z}^* = \mathbf{z}_{hf} + \Delta(\mathbf{z}_{lf} - \mathbf{z}_{hf}), \tag{14}$$

in which Δ is a uniformly distributed random variable with range $[0,1]$. An example of a perturbed state for turbulent channel flow ($Re_\tau = 640$) is given in Figure 5.

Based on the perturbed location $\mathbf{z}^*$ in the barycentric map, the new vector of eigenvalues ψ^* is computed as

$$\psi^* = \mathbf{B}^{-1}\mathbf{z}^*. \tag{15}$$

The associated perturbed anisotropy tensor is then computed as:

$$\mathbf{b}^* = \mathbf{E}\,\mathrm{diag}(\psi^*)\mathbf{E}^{-1}, \tag{16}$$

in which $\mathbf{E}$ is the matrix of eigenvectors of the unperturbed tensor $\mathbf{b}$. The tensors $\mathbf{T}^i$ and invariants π_i are computed based on the perturbed $\mathbf{b}^*$ and propagated through the model.

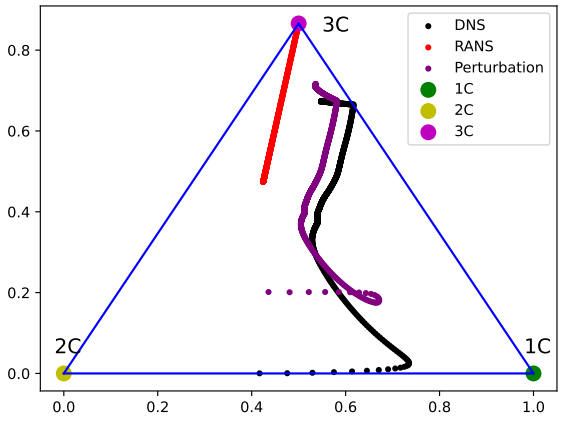

FIG. 5: Perturbed anisotropy state of turbulence in the barycentric map.

For each point of the original DNS dataset, 50 perturbed states are sampled and submitted to the data-driven models trained in single fidelity mode [18] and in the multi-fidelity mode described in section IV B. The predictions from both models are averaged, and confidence intervals are constructed to assess how uncertainties in the Reynolds stress components propagate through the data-driven closure.

E. Verification test case

To test the performance of the data-driven AHFMs generated with single fidelity [18] and multi-fidelity training modes, the networks were implemented in a CFD solver (OpenFoam) following the procedure proposed by Maulik et al. [37]. The test case proposed is a non-isothermal planar impinging jet simulated by Duponcheel et al. [30] at $Pr = 0.01$ for the geometry depicted in Figure 6.

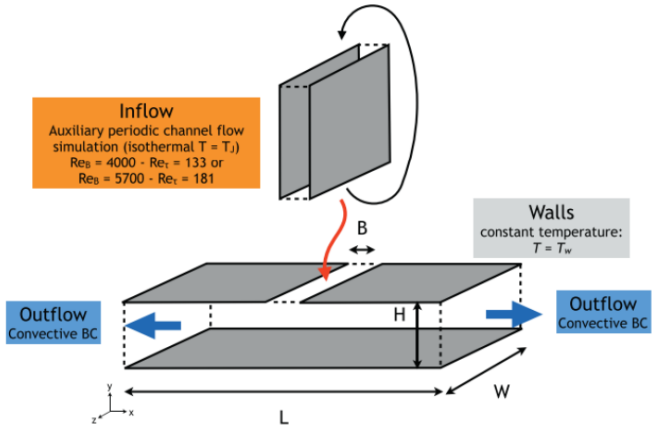

FIG. 6: Schematics of the impinging jet test case developed by Duponcheel et al. [30].

This test case is ideal for testing the data-driven closures, as this flow configuration is excluded from the training database. Additionally, for this flow configuration, the momentum field obtained with LEVMs (e.g., k-ε, k-ω) is affected by large uncertainties because of the the extent of anisotropy, secondary recirculation,and transport effects.

The computational domain for this test case consists of two infinite parallel plates with a slit in the middle injecting the flow conditions reached in a fully developed turbulent channel flow at $Re_\tau = 181$ (see Figure 7). The heat transfer is triggered by the temperature gap imposed on the walls. The structured computational grid leads to y^+ values ranging from 0.32 to 1.6 in the first cell near the wall, allowing a wall-resolved treatment for both momentum and thermal fields. The boundary conditions imposed are summarized in Table IV.

The simulations employed the Launder-Sharma k-ε and $k-\omega$ SST as turbulent momentum closures. The energy equation was closed with the analytical model developed by Manservisi [22], the original data-driven model introduced in section II

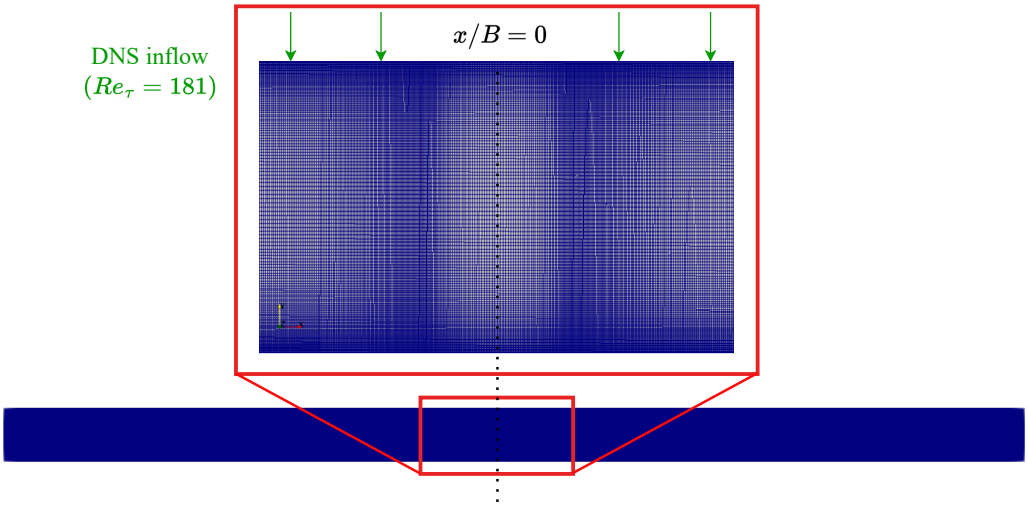

FIG. 7: Computational mesh used to simulate the planar impiging jet [30].

and the model generated with the multi-fidelity training mode.

V. RESULTS

This section presents the results of the analysis of the data-driven AHFM discussed in section II, comparing the model trained with multi-fidelity inputs to the one trained exclusively with DNS data. For brevity, we refer to the former as the *Hybrid* ANN and the latter as the *High-Fidelity* ANN.

A. Results of the PCA

The PCA was carried out on a feature matrix combining both the high-fidelity and the low-fidelity data.

The relevance of each principal component is illustrated in Figure 8, which also reports the cumulative sum of the variance explained. These results show that the first three principal components explain 77.5% of the total variance of the input data.

The loading matrix (eq. (9)) was computed to analyze the principal components' contribution to the original features' variance. The loadings of the first three principal components are shown in Figure 9. The loading values show that the first component (PC1) is mainly composed of momentum features depending on the mean velocity gradients and isotropic turbulence statistics (e.g., k, ε), which are similar in both RANS and DNS datasets. The second principal component (PC2) is primarily constituted by thermal-based features depending on the Prandtl number of the fluid. The third principal component (PC3) depends on momentum-based features that describe the turbulence anisotropy through the deviatoric part of the Reynolds stress tensor. These latter features are misrepresented in the RANS input dataset because of the Boussinesq approximation. Interestingly, the PCA algorithm splits the entire input dataset in three clusters, including isotropic momentum-based features (PC1), thermal-based features (PC2), and anisotropic momentum-based features (PC3).

The two datasets (RANS and DNS) are projected onto the PCs axes and compared in Figures 10 and 11. In particular, Figure 10 compares the two datasets in terms of PC1 and PC2. The DNS inputs achieve higher peaks of PC1 for the same PC2 values due to the higher turbulent kinetic energy retrieved in DNS simulations compared to the RANS counterpart. However, the distributions of the data on this plane are similar. A significant separation between the two datasets is observed when projected on the PC1 and PC3 plane, as done in Figure 11. This data separation reflects the effect of the Reynolds stress modeling and suggests that the current parameter space allows the detection of the type of momentum modeling based on the distance between critical features (mainly π_5 and π_3). This cluster separation is crucial to the present work, as it demonstrates that specific features constituting PC3 can be utilized by a data-driven algorithm to detect the fidelity level of the momentum turbulence model and to adapt predictions accordingly.

B. Performance of the training with multi-fidelity inputs

The neural network architecture introduced in section II was trained with the multi-fidelity approach introduced in section IV B. Specifically, for each value of α, 30 statistical trainings were carried out. The Pareto front of the multi-objective problem is reported in Figure 12, which is built from the final values achieved by the two losses at the end of each training. It is worth stressing that the resulting Pareto front is sharp, meaning that the training finds solutions that do not compromise the accuracy of the heat flux predictions with both types of inputs. This is an interesting result because it shows that increasing the robustness of the data-driven AHFM to momentum modeling is possible.

Regarding accuracy, a comparison between the hybrid ANN and the high-fidelity ANN is given in Figure 13, which

TABLE IV: Overview of boundary conditions imposed for all the variables for the RANS simulation of the non-isothermal planar impinging jet.

Field	Inlet	Outlet	Wall
$\mathbf{U}$	Mapped from DNS	$\frac{\partial U}{\partial n} = 0$ or $\mathbf{U} \cdot n = 0$	$\mathbf{U} = 0$
T	Fixed: $T = 2$	Adiabatic $\frac{\partial T}{\partial n} = 0$	Fixed: $T = 0$
p	$\frac{\partial p}{\partial n} = 0$	Fixed: $p = 0$	$\frac{\partial p}{\partial n} = 0$
k	Mapped from DNS	$\frac{\partial k}{\partial n} = 0$	$k = 0$
ε	Mapped from DNS	$\frac{\partial \varepsilon}{\partial n} = 0$	$\varepsilon = 0$
k_θ	$\frac{\partial k_\theta}{\partial n} = 0$	$\frac{\partial k_\theta}{\partial n} = 0$	$\frac{\partial k_\theta}{\partial n} = 0$
ε_θ	$\frac{\partial \varepsilon_\theta}{\partial n} = 0$	$\frac{\partial \varepsilon_\theta}{\partial n} = 0$	Manservisi wall function

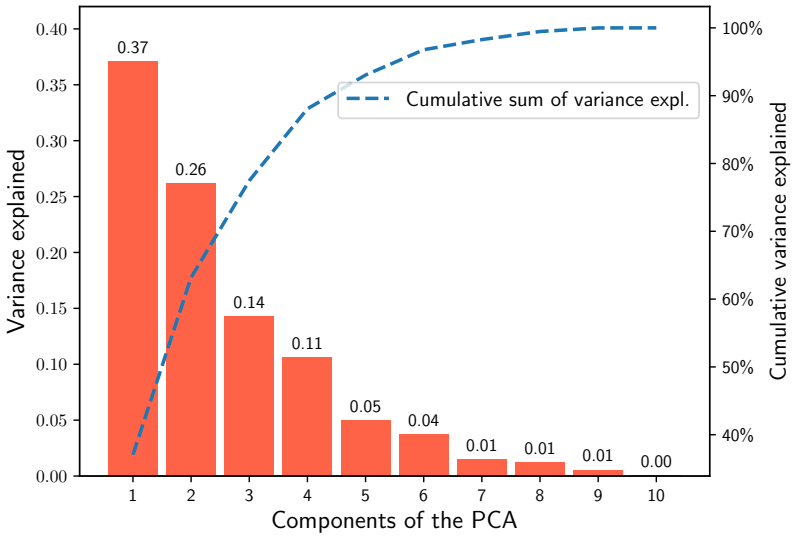

FIG. 8: Variance explained for each new PC. The blue dotted line represents the cumulative sum of each PC.

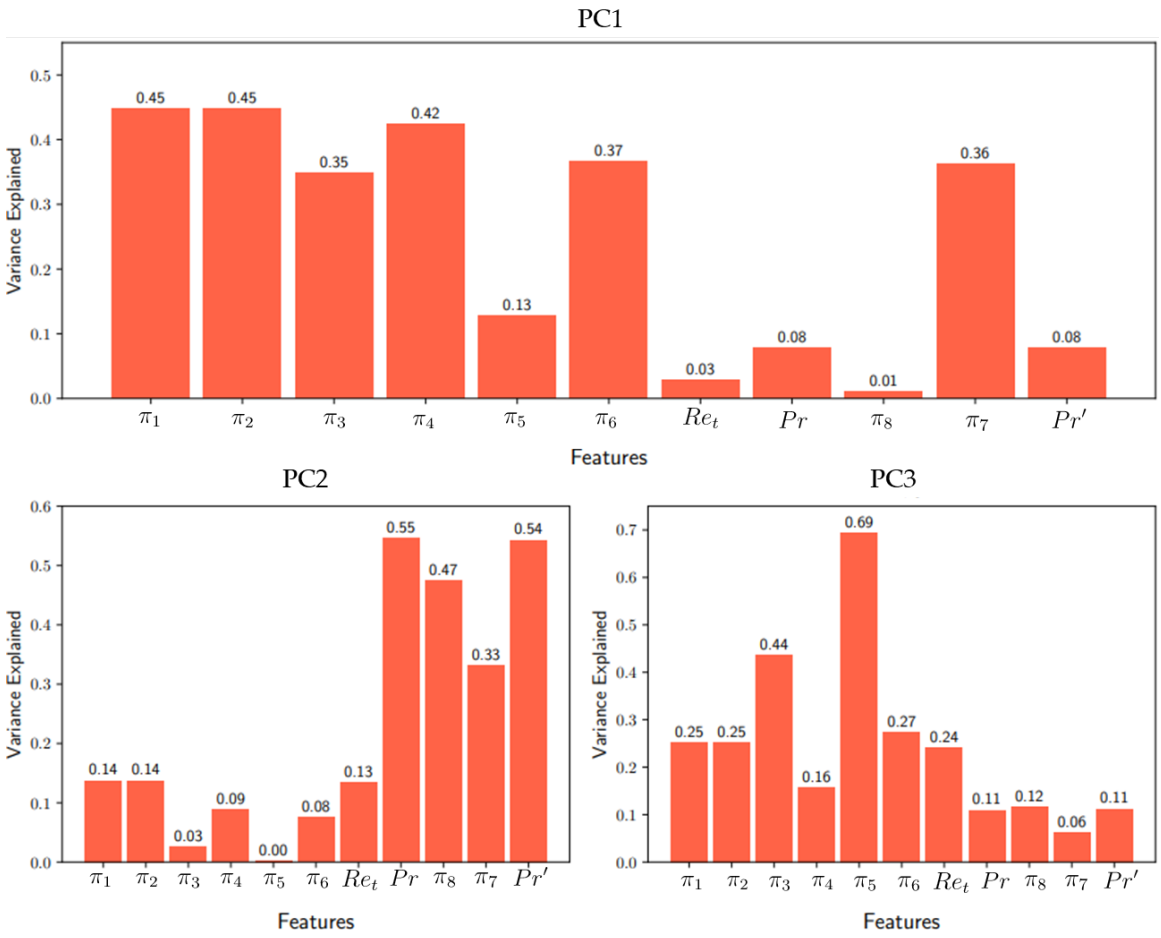

FIG. 9: Features variance explained by each Principal Component.

relates the network output obtained with DNS and RANS predictions. Note that hybrid ANN significantly reduces the dispersion of the heat flux predictions with the change of the momentum treatment.

C. Results of the sensitivity analysis

The Shapley values defined in eq.(11) were computed considering the streamwise and wall-normal components of the heat flux as the outputs of the model in the case of non-isothermal turbulent channel flow. Figures 14 and 15 presents the obtained Shapley values for the hybrid network at $Pr = 0.71$ and $Pr = 0.025$, respectively. The values obtained in the presence of DNS inputs are indicated with solid lines and those of RANS inputs with dashed lines. At near-unity Prandtl numbers, the data-driven model is shown to be highly sensitive to the thermal features. This sensitivity reduces at $Pr = 0.025$, which means that the dependence of the model on thermal gradients and features increases with the Prandtl number. This effect is primarily attributed to the lower dependency of the heat flux on the temperature gradient at low Prandtl numbers, which is a consequence of the break-up of the similarity hypothesis and the single-point modeling assumption discussed in other works on this topic [38, 39]. Clearly, the ANN trained with the multi-fidelity approach is insensitive to the anisotropy-based invariants in the presence of RANS inputs. However, it preserves a small sensitivity to this group when the model is fed with high-fidelity momentum data.

Comparison of Shapley values in the presence of DNS and RANS data (Figure 14 and 15) shows that the sensitivity of the model to certain groups of features appears to decrease when low-fidelity data are detected. In addition to the MA group, this is also true for the TE and TH groups for the stream-wise component in Figures 14 and 15. The profiles of the Shapley values over the channel width also indicate that the hybrid model tends to be less sensitive to small gradients when low-fidelity data are detected, as lower peaks and fewer sign changes characterize the profiles depicted with dashed lines. Since the differences in input are moderate for the MI and TH groups, this trend seems to indicate a specific behavior of the model depending on the input type.

Figure 16 shows the distribution of the Shapley values of the original high-fidelity ANN for the same flow configuration at $Pr = 0.71$. For the same input (DNS) data, the comparison between the Shapley values of the two networks is presented in Figure 17 for the streamwise heat flux component at $Pr = 0.71$. A similar comparison for the wall-normal

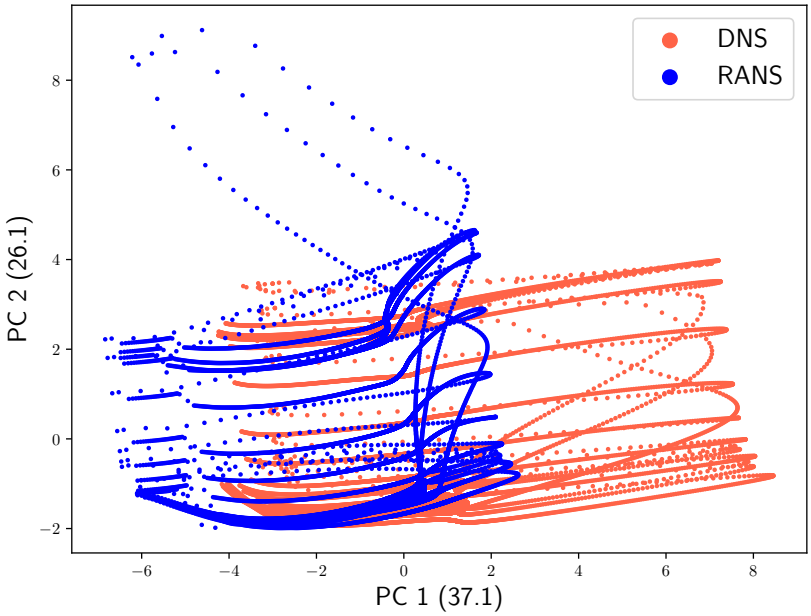

FIG. 10: Projection of the RANS and DNS input data referred to non-isothermal turbulent channel flow onto the PC1 and PC2 axes.

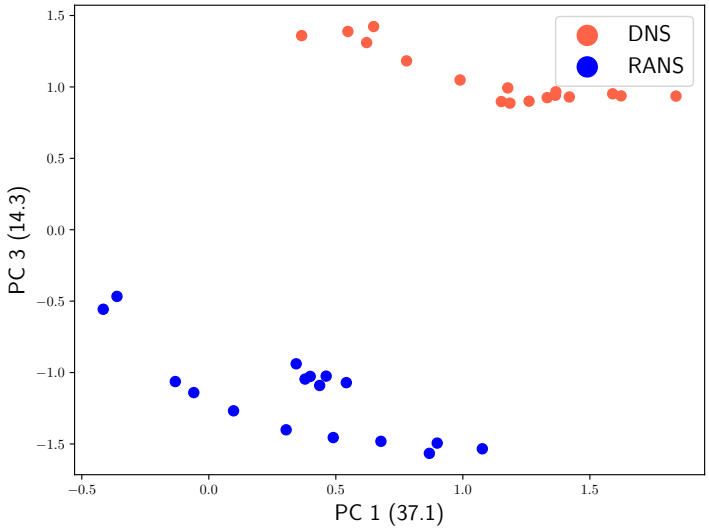

FIG. 11: Projection of the RANS and DNS input data referred to non-isothermal turbulent channel flow onto the PC1 and PC3 axes.

component is reported for completeness in Appendix A. Figure 17 shows a reduced sensitivity of the hybrid network to the MA and TE groups defined in Table III, which depend on the anisotropic part of the Reynolds stresses. The decrease in sensitivity is especially evident for $y^+ \approx 10$, where the turbulent momentum production peaks. The barycentric triangle in Figure 4 shows that the gap between the turbulent RANS and DNS states is maximum at this distance from the wall. Hence, the hybrid training mode moderates the sensitivity to the anisotropic part of the Reynolds stresses, where the separation between the two categories of inputs is significant. The sensitivity to the TE and MA groups appears compensated for

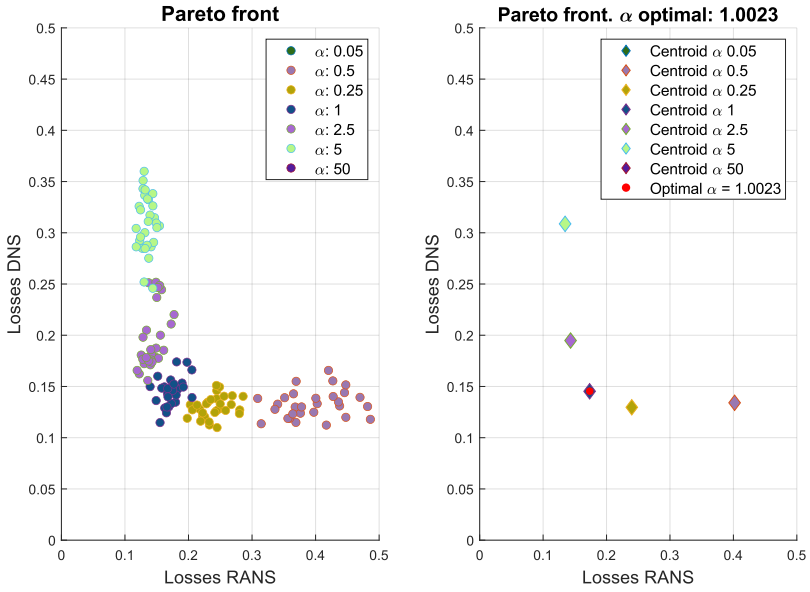

FIG. 12: Pareto Front obtained by training the network 30 times for each value of α. On the left, the entire ensemble of losses is depicted. The centroids obtained for each value of α are shown on the right.

by a higher sensitivity to the MI group, consisting of momentum isotropic features. This confirms that this training strategy effectively leads to a more robust thermal model with respect to the one trained with high-fidelity data only, which would better interface with standard momentum closures based on the eddy viscosity concept.

D. Layer output analysis

Additional insights into the differences between the models obtained from the single-fidelity and multi-fidelity training can be obtained by analyzing the output layer of the network schematized in Figure 1. Figure 18 depicts the coefficients a_i and w_i at the output of the merged layer (see Figure 1) of the ANN trained with the multi-fidelity approach, in case of non-isothermal turbulent channel flow at $Re_\tau = 640$ and $Pr = 0.025$ and with high-fidelity and low-fidelity momentum input data.[40]. For both types of input data, the dominant coefficients are a_1, a_2, a_6, w_4, and w_6. For $y^+ > 100$, the values of the predicted coefficients are similar for both DNS and RANS inputs. At $y^+ \simeq 10$, where the turbulence anisotropy reaches its peak, the predicted coefficients are much higher in the presence of DNS input data than in the presence of RANS inputs. This explains the lower sensitivity to the RANS inputs detected by the Shapley value analysis in Section V C. The reduction is significant, especially for a_2, the coefficient multiplying the tensor $\mathbf{T}_2$ that is proportional to the anisotropic part of the Reynolds stress tensor $\mathbf{b}$, as reported in Table I.

The output of the last layer of the high-fidelity network is significantly different, as shown in Figure 19. The coefficients a_1 and a_2 dominate above all the other terms and achieve a single peak in the region of maximum momentum turbulence production ($y^+ \approx 10$). Hence, compared to the high-fidelity network, the new model increases the dependence on $\mathbf{T}_4$, $\mathbf{T}_6$, and $\mathbf{T}_8$ which depend on the strain and rotation tensors. This implies that training the network with data of multiple fidelity replaces the dependence on the true Reynolds stress tensor with linear and quadratic functions of the velocity gradient. In other words, the network tries to reconstruct the true Reynolds stress anisotropy as a function of the mean velocity gradient and its uncertain estimate given by the combined momentum turbulence model. This explains the low dispersion of the predictions shown in Figure 13 with both kinds of momentum treatments.

E. Propagated uncertainties

The uncertainties of the Reynolds stress tensor caused by the inaccuracies of the combined momentum treatment were propagated to the output of the data-driven AHFM with the method explained in section IV D. The statistics obtained for $Re_\tau = 640$ and $Pr = 0.71$ and 0.025 are shown in figures 20 and 21, respectively. The confidence intervals, highlighted with shaded areas, quantify the uncertainty of the predictions due to the inconsistency between reference and modeled input data. The comparison between the hybrid ANN and the high-fidelity ANN reveals a significant reduction of the model uncertainty when the training is enriched with RANS data. This is true at both near unity and low Prandtl numbers, albeit more evident for $Pr = 0.71$, at which a stronger dependence of the heat flux field on the Reynolds stresses is expected.

The standard deviation computed for the two models at both values of the Prandtl numbers is shown in Figure 22. The standard deviation of the high-fidelity model achieves its peak

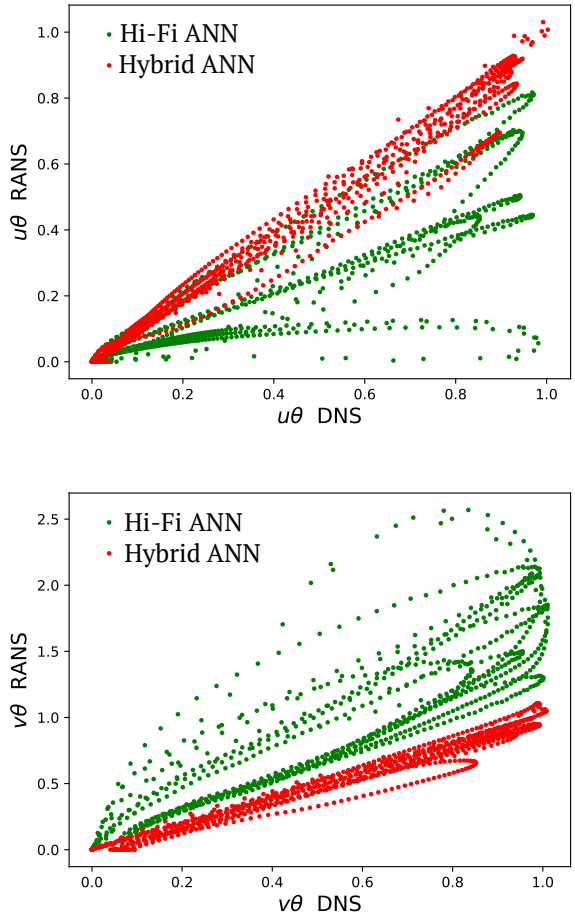

FIG. 13: Comparison between the predictions with the two types of input data given by the trained ANNs, i.e. the data-driven AHFM trained with high-fidelity data ($\alpha = 0$) and the same model trained with the hybrid DNS-RANS dataset ($\alpha = 1.0$). The dataset consists of non isothermal turbulent channel flows at different Reynolds and Prandtl numbers.

in the near-wall region, where the dependence of the model on the anisotropy state is maximum. In this region, the standard deviation of the predictions of the hybrid model is much lower since training with both types of data mitigates the dependence on Reynolds stress anisotropy. This evidence agrees with the considerations drawn for the Shapley values for y^+ close to 10.0. This region of peak turbulence production, where temperature gradients are most significant and the influence of the temperature field on heat flux is at its maximum, is critical. Therefore, reducing the uncertainty in model predictions in this area is of utmost importance. These considerations lead to the conclusion that the hybrid ANN is substantially more robust than the high-fidelity ANN in managing inaccuracies within the combined momentum turbulence model.

F. Results of the simulation test case

The numerical setup described in Section IV E was employed to verify the behavior of the hybrid model when combined with LEVMs, and to compare the new formulation with the original data-driven AHFM. As anticipated in section IV E, for this test case, the computed velocity field highly depends on the type of momentum treatment and the choice of the specific LEVM. This is confirmed in Figure 23, which presents the velocity fields computed with the $k-\varepsilon$ and $k-\omega$ models. The size and shape of the recirculation bubble generated after the impinging point significantly differ from the two closure models. The difference can also be seen from the velocity and k profiles reported in Figures 24 and 25, where they are compared to the reference DNS. In particular, the $k-\varepsilon$ and $k-\omega$ models underestimate and overestimate the extension of the recirculation bubble.

The data-driven thermal model and the Manservisi model [22] were applied to the two underlying momentum fields to calculate the heat flux and temperature distributions. The resulting wall-normal heat flux profiles at several distances from the impinging point are shown by Figure 26. The high-fidelity ANN, whose predictions are indicated with dashed blue lines, completely mismatches the reference heat flux profiles due to the inconsistency between training (DNS) and simulation (RANS) momentum data. The hybrid ANN gives more accurate heat flux predictions, regardless of the combined momentum closure ($k-\varepsilon$ or $k-\omega$). These results show that the applicability of the hybrid ANN is not restricted to the momentum closure that generated the training data (Launder-Sharma $k-\varepsilon$), but could potentially extend to the entire LEVM family. A comparison of the different thermal closures is provided in Figure 27. The Figure plots the averaged heat flux error over the impinging wall, here defined as:

$$e = \frac{1}{L_y}\int_{y_{min}}^{y_{max}} \frac{\overline{v\theta}_{DNS} - \overline{v\theta}}{\max_y(\overline{v\theta}_{DNS})} dy, \tag{17}$$

with L_y the channel's height. The comparison shows the superiority of the hybrid network with respect to the High-fidelity network, as the maximum average error is around 10% for the hybrid network. At the same time, it is higher than 20% for the high-fidelity network. When coupled with the $k-epsilon$ momentum turbulence model, the hybrid network is also more accurate than the Manservisi model over the entire impinging wall.

The comparison among the thermal models in terms of temperature distribution is presented in Figure 28, in which the hybrid ANN combined with the $k-\omega$ SST shows the best accuracy. In contrast, the hybrid ANN and the Manservisi model significantly overestimate the temperature, especially far from the slit. However, the better thermal field computed with the $k-\omega$ and hybrid ANN does not originate from a significantly more accurate heat flux modeling. Indeed, the comparison of the profiles in Figure 26 indicate a higher accuracy of the hybrid network combined with the $k-\varepsilon$ turbulence model. The better temperature agreement achieved with the high-fidelity ANN compared to the hybrid ANN, using the same momentum closure, suggests that the temperature field results from

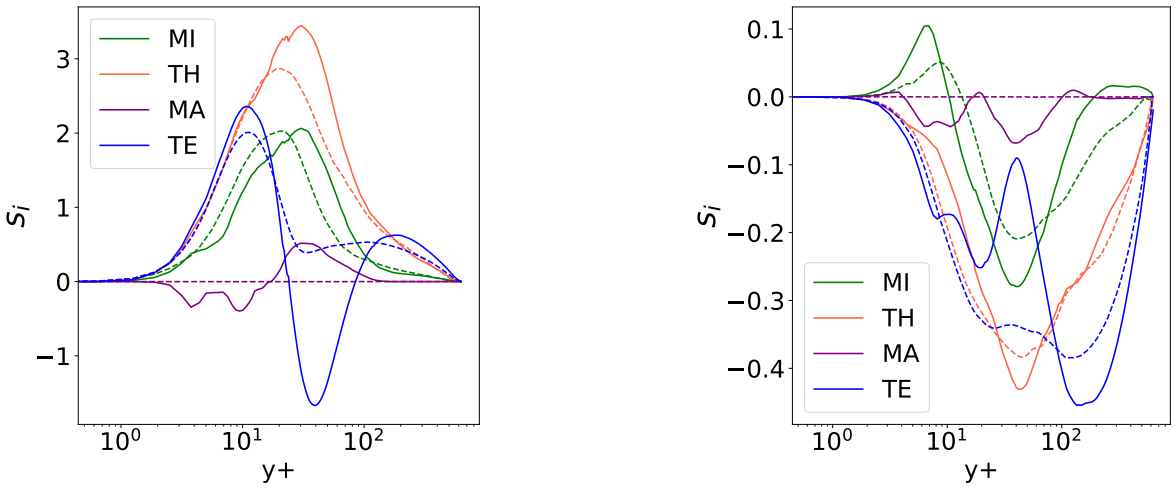

FIG. 14: Shapley values of the groups indicated in Table III for the streamwise (left) and wall normal (right) heat flux in presence of non-isothermal turbulent channel flow at $Re_\tau = 640$ and $Pr = 0.71$. The values obtained with DNS and RANS input data are indicated with solid and dashed lines, respectively. Results obtained with the hybrid network.

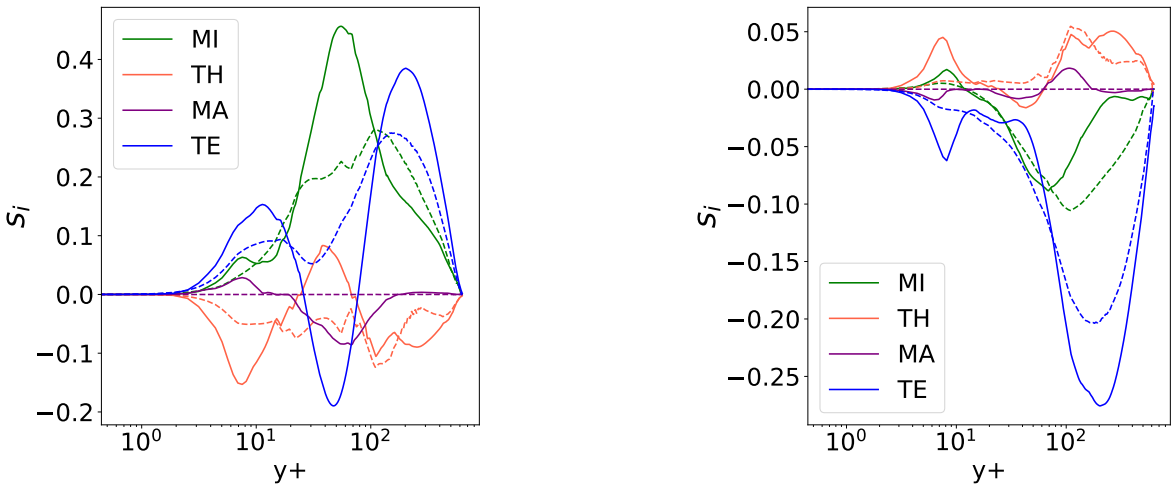

FIG. 15: Shapley values of the groups indicated in Table III for the streamwise (left) and wall normal (right) heat flux in presence of non-isothermal turbulent channel flow at $Re_\tau = 640$ and $Pr = 0.025$. The values obtained with DNS and RANS input data are indicated with solid and dashed lines, respectively. Results obtained with the hybrid network.

compensation of errors in both the momentum and thermal closures. Such compensation is suggested by the inaccuracies in the velocity profiles depicted in Figure 24, which also affect the computed temperature. This consideration further underlines the importance of combining accurate thermal and momentum closures for heat transfer RANS simulations, as both the turbulent treatments contribute substantially to the resulting thermal field. This is especially true for low Prandtl numbers, at which the turbulent heat transport can be comparable, or even lower, than molecular transport and convection contributions in the overall energy balance.

VI. CONCLUSIONS AND OUTLOOK

This article investigated the problem of model-data inconsistency for a data-driven thermal turbulence model trained with high-fidelity data. Specifically, we explored ways to improve the robustness of the data-driven model to extend its coupling with low-fidelity models for Reynolds stresses

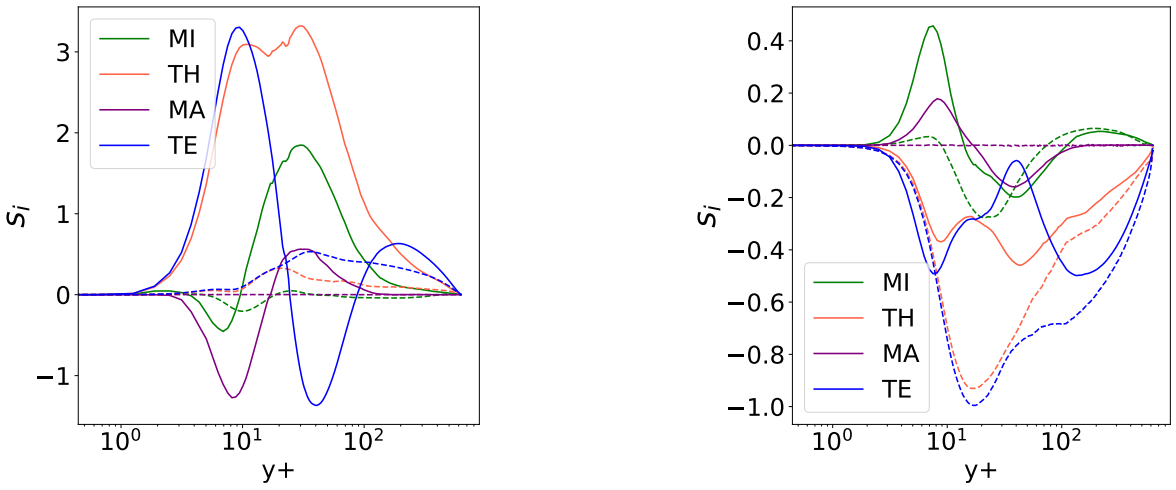

FIG. 16: Shapley values of the groups indicated in Table III for the streamwise (left) and wall normal (right) heat flux in presence of non-isothermal turbulent channel flow at $Re_\tau = 640$ and $Pr = 0.025$. The values obtained with DNS and RANS input data are indicated with solid and dashed lines, respectively. Results obtained with the Hi-Fi network.

(LEVMs), generally preferred in industrial contexts for their stability and computational cost.

The crucial point was understanding whether the modeled (RANS) input statistics could be employed in training to inform the data-driven model about the inconsistencies between low and high-fidelity data. Detecting the quality of the momentum treatment could allow to adapt to different inputs or mitigate the sensitivities to the most critical ones. For such purpose, the work proposes the analysis of the multi-fidelity input space and a training strategy based on a hybrid dataset consisting of DNS and RANS input data.

The work demonstrates that increasing the robustness of the thermal model with respect to momentum modeling is possible. The systematic deviation between high-fidelity and low-fidelity statistics can be utilized to identify the type of momentum modeling and adapt the output accordingly or to find alternative relationships of the input statistics. The multi-fidelity training mode generates a model less sensitive to Reynolds stress anisotropy than the model trained with only high-fidelity data, especially in regions characterized by high anisotropy. The network naturally adapts its sensitivity to low-fidelity inputs (RANS) and is thus more robust than the original. From a structural standpoint, the hybrid model appears to incorporate Reynolds stress anisotropy modeling through algebraic expansions of tensors dependent on velocity gradients (strain and rotation tensors).

The validation of the new data-driven model for a non-isothermal planar impinging jet shows that it is significantly more robust than the original high-fidelity network and provides accurate predictions with different eddy viscosity models. The uncertainty propagation analysis demonstrates, more generally, the greater robustness of the new model against perturbations of the Reynolds stresses in the barycentric plane.

While more test cases are needed to develop a truly general-purpose model, the promising results of this work open the door to new training strategies for data-driven turbulence closures that can leverage information from databases of varying sizes and fidelity levels. As demonstrated here, multi-fidelity inputs enhance model robustness and resilience to perturbations of input statistics. Additionally, incorporating multi-fidelity targets can expand the training database to include conditions where high-fidelity data are challenging to obtain, such as high Reynolds or Grashof numbers or flows involving multiple physics or complex geometries. This approach can improve the generality and applicability of the learned closures. Future work will focus on extending the current framework to a broader range of data, both in inputs and outputs, to further advance data-driven turbulence modeling and its application in industrial contexts.

NOMENCLATURE

$\mathbf{U}$	[m/s]	Mean velocity
T	[K]	Mean Temperature
$\mathbf{u}$	[m/s]	Velocity fluctuation
θ	[K]	Thermal fluctuation
k	[m^2/s^2]	Turbulent kinetic energy
ε	[m^2/s^3]	Turbulent dissipation rate
k_θ	[K^2]	Thermal variance
ε_θ	[K^2/s]	Thermal dissipation rate
$\overline{\mathbf{uu}}$	[m^2/s^2]	Reynolds stress

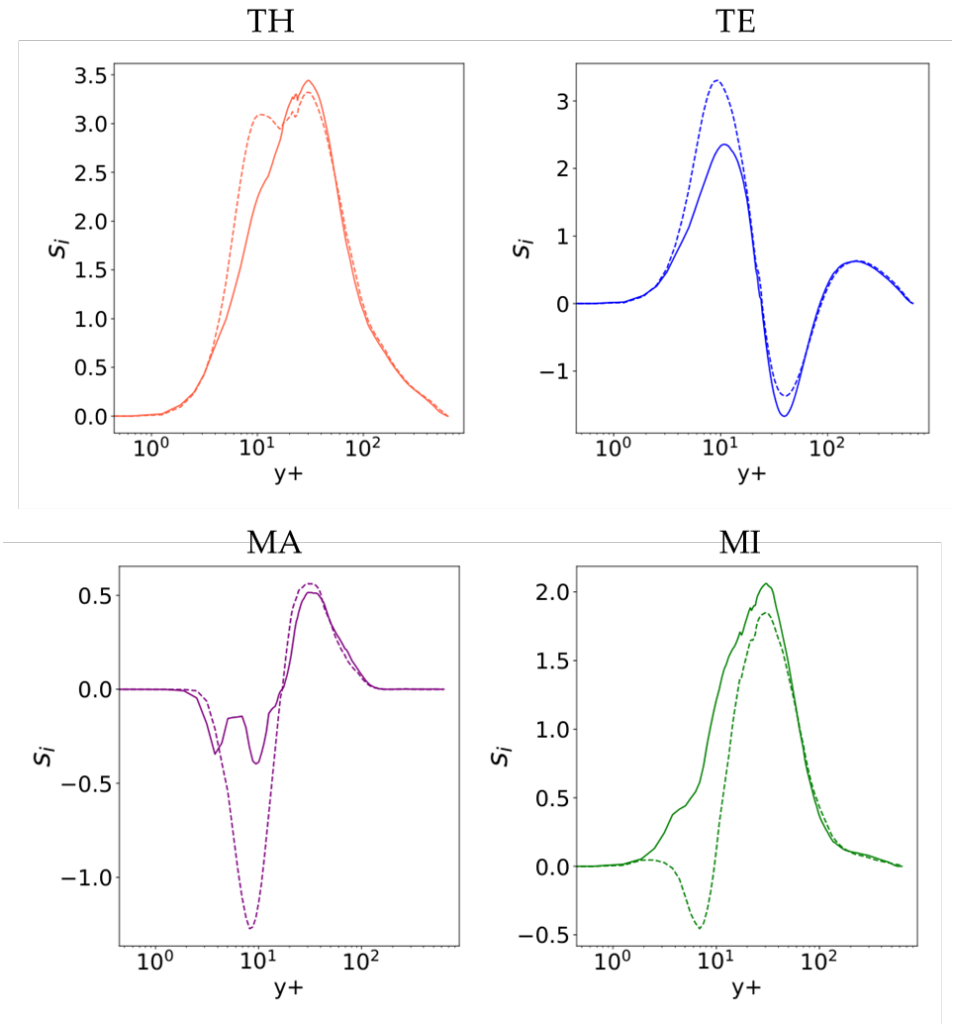

FIG. 17: Comparison between the Shapley values obtained for the Hi-Fi network (dashed line) and hybrid network (solid line) for the streamwise component of the heat flux at $Pr = 0.71$.

$\overline{\mathbf{u}\theta}$	[mK/s]	Turbulent heat flux
ν	[m^2/s]	Molecular viscosity
α_l	[m^2/s]	Molecular diffusivity
δ	[m]	Half channel width
$\mathbf{I}$	[-]	Identity tensor
$\mathbf{S}$	[1/s]	Strain rate tensor
$\mathbf{\Omega}$	[1/s]	Rotation tensor
$\mathbf{b}$	[-]	Reynolds stress anisotropy tensor

ACRONYMS

CFD	Computational Fluid Dynamics
RANS	Reynolds Averaged Navier-Stokes
DNS	Direct Numerical Simulation
ANN	Artificial Neural Network
AHFM	Algebraic Heat Flux Model
EBRSM	Elliptic Blending Reynolds Stress Model
LEVM	Linear Eddy Viscosity Model
PCA	Principal Component Analysis

ACKNOWLEDGMENTS

This work was supported by an F.R.S.-FNRS FRIA grant, and partially funded by the European Commission in the framework of the collaborative projects ANSELMUS-101061185. The authors gratefully acknowledge Prof. Iztok Tiselj and Dr. Mathieu Duponcheel for providing their datasets.

Appendix A: Shapley values of wall-normal heat flux

This section completes the comparison of the Shapley values presented in section V C for non-isothermal turbulent channel flow. Figure 29 presents the Shapley values computed for the wall-normal component of the heat flux at $Pr = 0.71$. For each group of features, the values obtained for the Hi-Fi network are depicted with dashed lines, for the hybrid network with solid lines. Similar conclusions to the ones expressed in

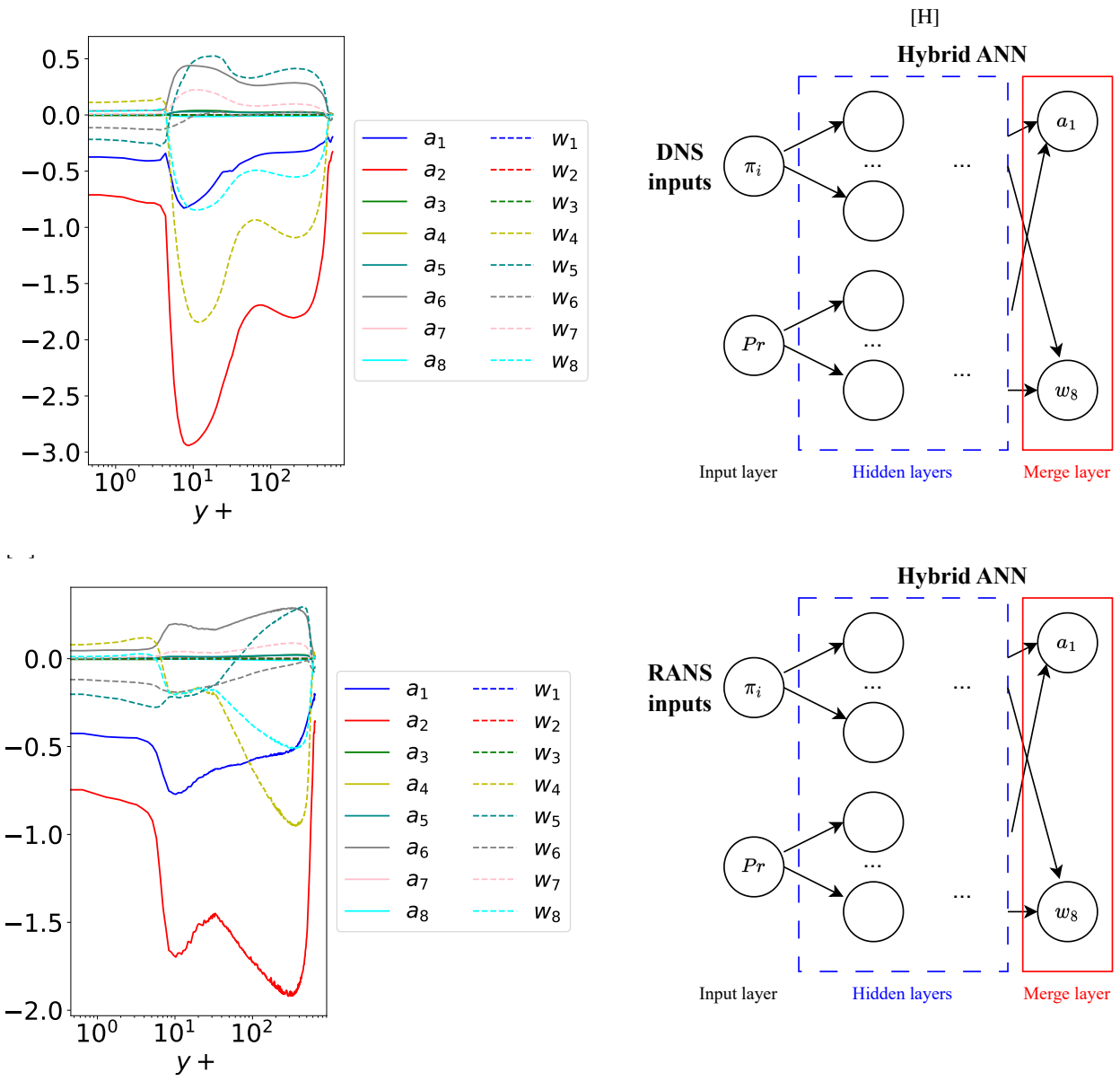

FIG. 18: Output of the merge layer of the hybrid ANN for DNS (up) and RANS (bottom) inputs in case of non-isothermal turbulent channel flow at $Re_\tau = 640$ and $Pr = 0.025$.

section V C can be drawn from the results obtained for the two networks.

Appendix B: RANS setup for the training flows

The simulations of the RANS counterpart of the flows in the training database were conducted in the openfoam environment with the Launder-Sharma k-ε model. The choice of the computational domains follow the setups described in Ref. [27] and [29]. For both setups, the mesh is structured and consistent with the wall-resolved approach, i.e., the values of y^+ range between 0.1 and 1.0. Table VI and V indicate the boundary conditions applied for the two flows.

For the channel, the fully developed flow is obtained by imposing cyclic boundary conditions at the inlet and outlet and a pressure gradient source term that adapts to the bulk velocity prescribed. For the backward-facing step flow, a fully developed flow in the channel preceding the step is obtained using recycling conditions, i.e., the iterative remapping of the fields at a certain distance from the inlet to the inlet boundary.

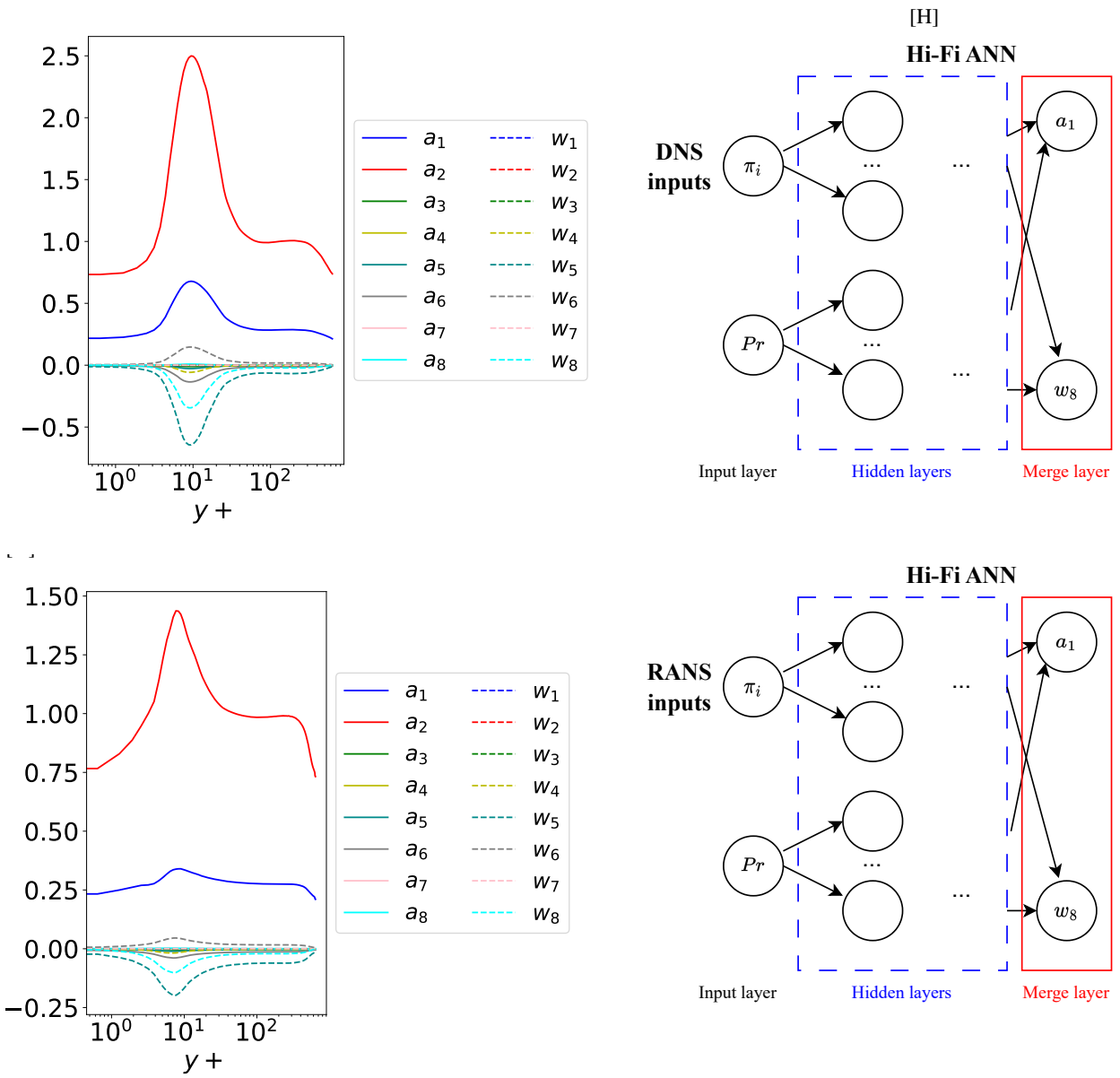

FIG. 19: Output of the merge layer of the Hi-Fi ANN for DNS (up) and RANS (bottom) inputs in case of non-isothermal turbulent channel flow at $Re_\tau = 640$ and $Pr = 0.025$.

[1] J. Ling, A. Kurzawski, and J. Templeton, Reynolds averaged turbulence modelling using deep neural networks with embedded invariance, Journal of Fluid Mechanics **807**, 155 (2016).

[2] C. Jiang, R. Vinuesa, R. Chen, J. Mi, S. Laima, and H. Li, An interpretable framework of data-driven turbulence modeling using deep neural networks, Physics of Fluids **33**, 055133 (2021).

[3] Y. Yin, Z. Shen, Y. Zhang, H. Chen, and S. Fu, An iterative data-driven turbulence modeling framework based on reynolds stress representation, Theoretical and Applied Mechanics Letters **12**, 100381 (2022).

[4] R. McConkey, E. Yee, and F.-S. Lien, On the generalizability of data-driven turbulence closure models, arXiv preprint arXiv:2206.05226 (2022).

[5] N. Geneva and N. Zabaras, Quantifying model form uncertainty in reynolds-averaged turbulence models with bayesian deep neural networks, Journal of Computational Physics **383**, 125 (2019).

[6] S. Berrone and D. Oberto, An invariances-preserving vector basis neural network for the closure of reynolds-averaged navier–stokes equations by the divergence of the reynolds stress tensor, Physics of Fluids **34** (2022).

[7] J. Cai, P.-E. Angeli, J.-M. Martinez, G. Damblin, and D. Lu-

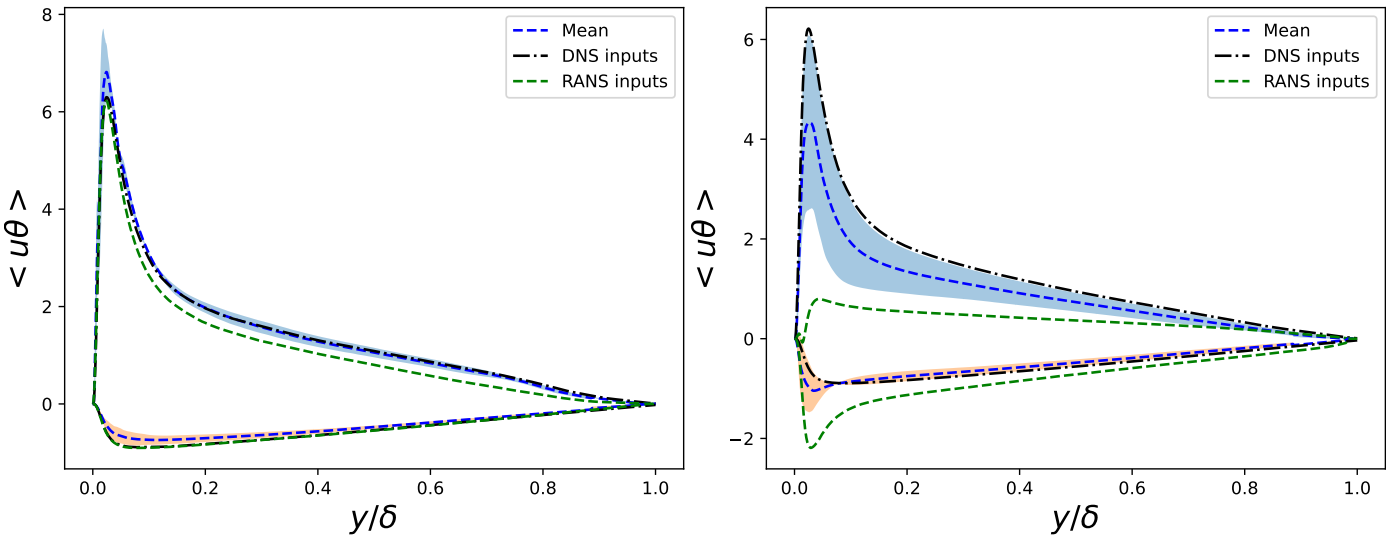

(a) Hybrid ANN (b) Hi-Fi ANN

FIG. 20: Predictions of the turbulent heat flux components given by the hybrid and Hi-Fi ANNs with both the kind of inputs for non-isothermal turbulent channel flow at $Re_\tau = 640$ and $Pr = 0.71$. The model predictions' confidence intervals (2σ) due to the model-data inconsistency are indicated with shaded areas.

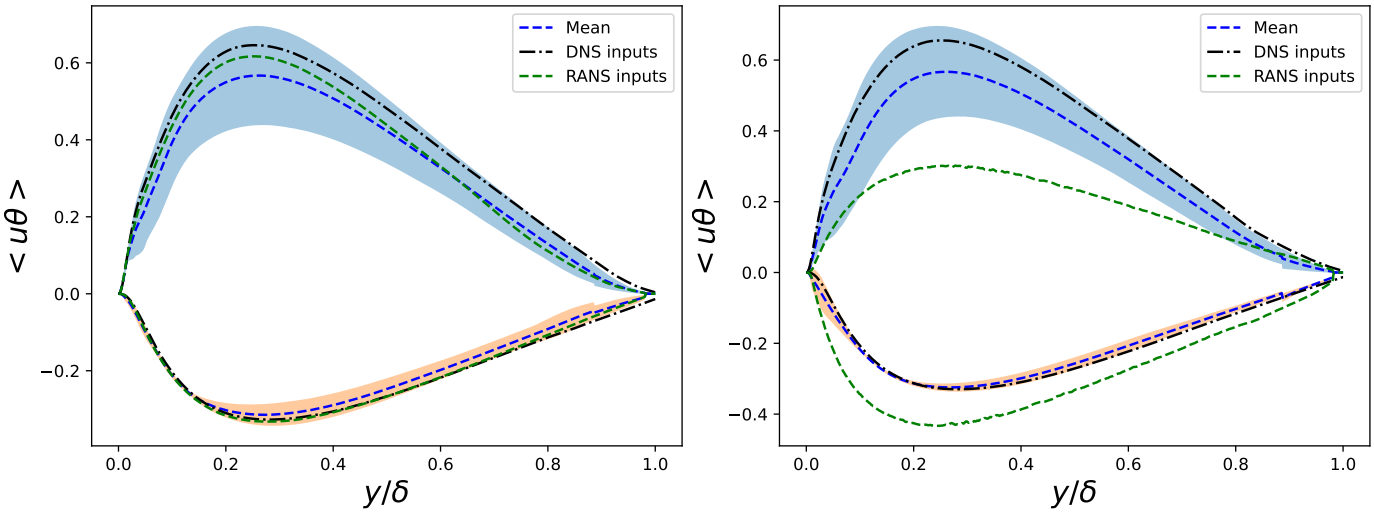

(a) Hybrid ANN (b) Hi-Fi ANN

FIG. 21: Predictions of the turbulent heat flux components given by the hybrid and Hi-Fi ANNs with both the kind of inputs for non-isothermal turbulent channel flow at $Re_\tau = 640$ and $Pr = 0.025$. The model predictions' confidence intervals (2σ) due to the model-data inconsistency are indicated with shaded areas.

TABLE V: Overview of the boundary conditions imposed for the RANS simulation of the backward facing step.

Field	Inlet	Outlet	Walls
$\mathbf{U}$	Recycling	$\frac{\partial \mathbf{U}}{\partial n} = 0$ or $\mathbf{U} \cdot n = 0$	$\mathbf{U} = 0$
p	$\frac{\partial p}{\partial n} = 0$	Fixed: $p = 0$	$\frac{\partial p}{\partial n} = 0$
k	Recycling	$\frac{\partial k}{\partial n} = 0$	$k = 0$
ε	Recycling	$\frac{\partial \varepsilon}{\partial n} = 0$	$\varepsilon = 0$
$\overline{\mathbf{uu}}$	Recycling	$\frac{\partial \overline{\mathbf{uu}}}{\partial n} = 0$	$\overline{\mathbf{uu}} = 0$

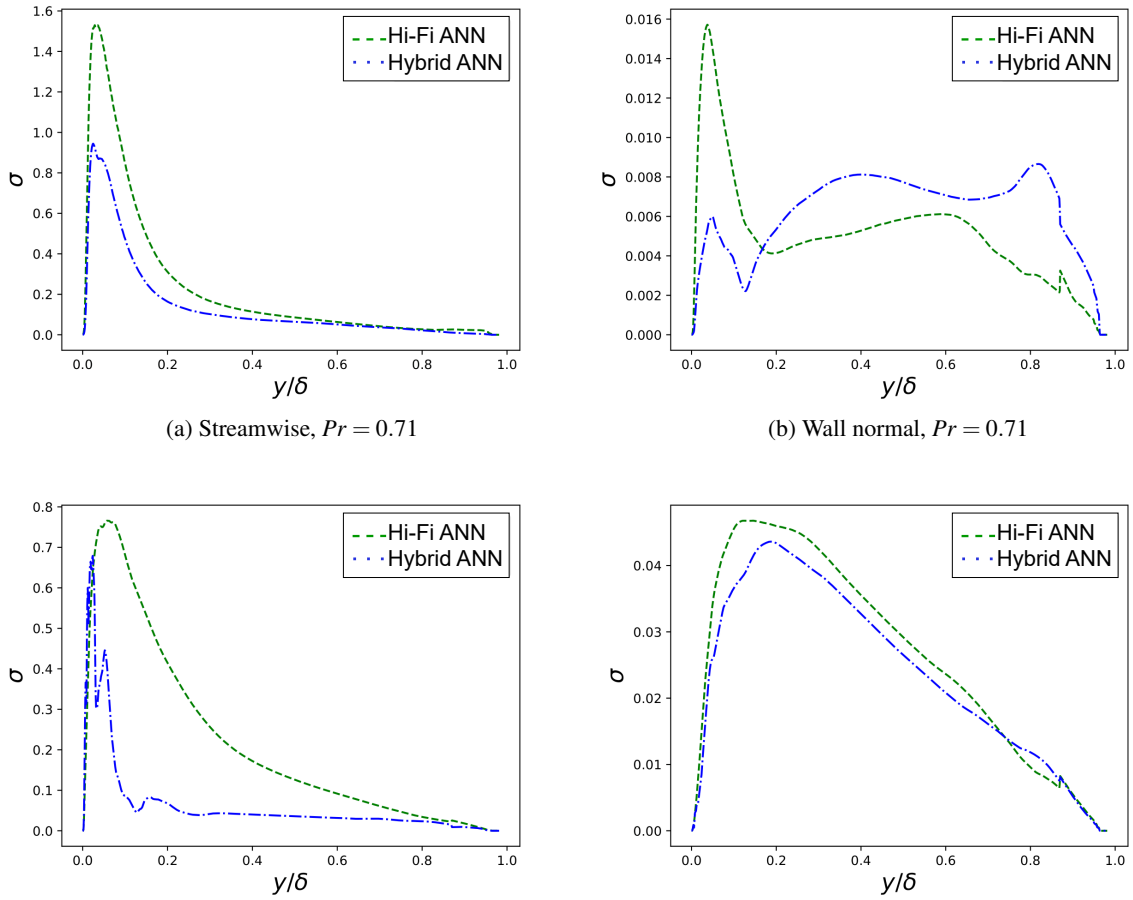

(a) Streamwise, $Pr = 0.71$

(b) Wall normal, $Pr = 0.71$

(c) Streamwise, $Pr = 0.025$

(d) Wall normal, $Pr = 0.025$

FIG. 22: Distribution of the standard deviation of the streamwise and wall-normal heat flux components estimated by perturbing the true anisotropy turbulent state.

cor, Revisiting tensor basis neural network for reynolds stress modeling: Application to plane channel and square duct flows, Computers & Fluids **275**, 106246 (2024).

[8] C. Sotgiu, B. Weigand, K. Semmler, and P. Wellinger, Towards a general data-driven explicit algebraic reynolds stress prediction framework, International Journal of Heat and Fluid Flow **79**, 108454 (2019).

[9] Y. Zhang, D. Zhang, and H. Jiang, Review of challenges and opportunities in turbulence modeling: A comparative analysis of data-driven machine learning approaches, Journal of Marine Science and Engineering **11**, 1440 (2023).

[10] V. Srivastava and K. Duraisamy, Generalizable physics-constrained modeling using learning and inference assisted by feature-space engineering, Physical Review Fluids **6**, 124602 (2021).

[11] P. M. Milani, *Machine learning approaches to model turbulent mixing in film cooling flows* (Stanford University, 2020).

[12] Y. Zhao, H. D. Akolekar, J. Weatheritt, V. Michelassi, and R. D. Sandberg, Rans turbulence model development using cfd-driven machine learning, Journal of Computational Physics **411**, 109413 (2020).

[13] S. S. Girimaji, Turbulence closure modeling with machine learning approaches: A perspective, arXiv preprint arXiv:2312.14902 (2023).

[14] H. Mandler and B. Weigand, On frozen-rans approaches in data-driven turbulence modeling: Practical relevance of turbulent scale consistency during closure inference and application, International Journal of Heat and Fluid Flow **97**, 109017 (2022).

[15] M. Schmelzer, R. P. Dwight, and P. Cinnella, Discovery of algebraic reynolds-stress models using sparse symbolic regression, Flow, Turbulence and Combustion **104**, 579 (2020).

[16] J. Weatheritt and R. D. Sandberg, The development of algebraic stress models using a novel evolutionary algorithm, International Journal of Heat and Fluid Flow **68**, 298 (2017).

[17] M. Fiore, L. Koloszar, M. A. Mendez, M. Duponcheel, and Y. Bartosiewicz, Turbulent heat flux modelling in forced convection flows using artificial neural networks, Nuclear Engineering and Design **399**, 112005 (2022).

[18] M. Fiore, L. Koloszar, C. Fare, M. A. Mendez, M. Duponcheel, and Y. Bartosiewicz, Physics-constrained machine learning for thermal turbulence modelling at low prandtl numbers, International Journal of Heat and Mass Transfer **194**, 122998 (2022).

[19] B. J. Daly and F. H. Harlow, Transport equations in turbulence, The physics of fluids **13**, 2634 (1970).

[20] K. Suga and K. Abe, Nonlinear eddy viscosity modelling for

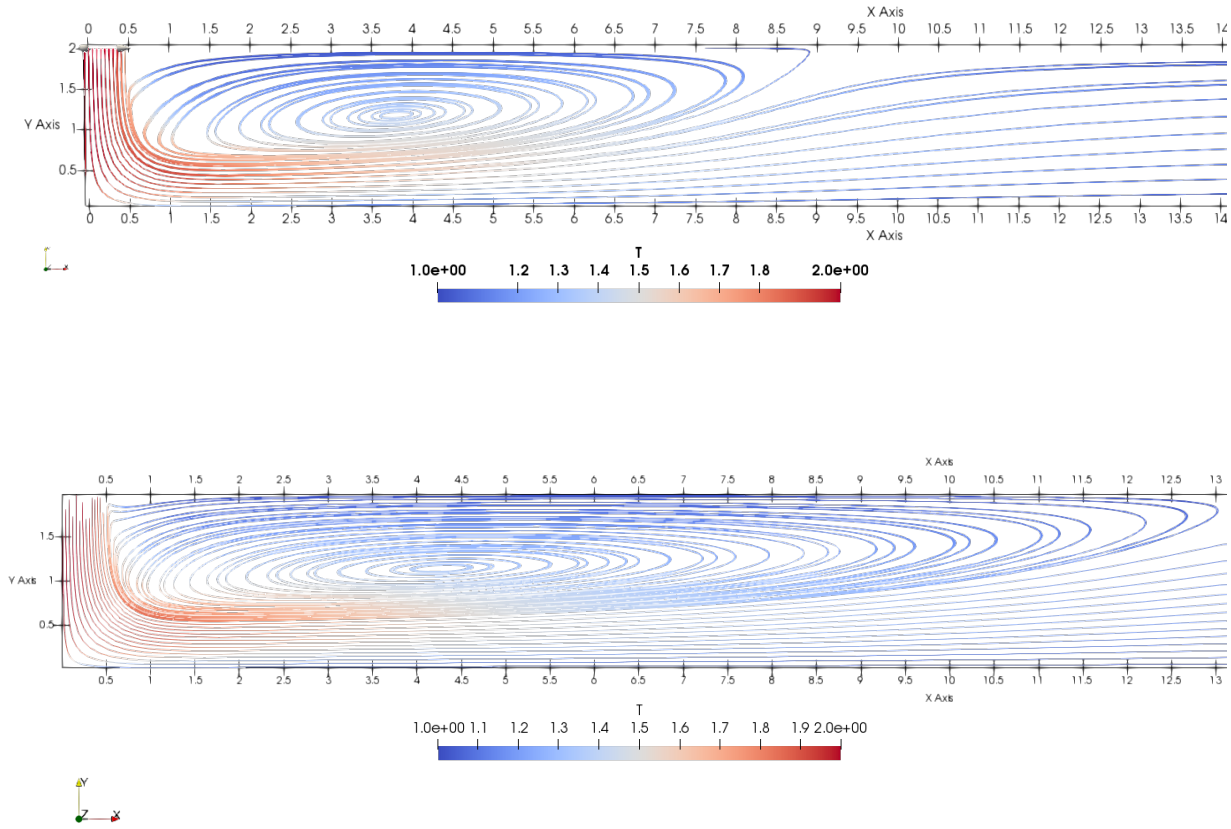

FIG. 23: Shape of the recirculation bubble obtained with the Launder-Sharma $k-\varepsilon$ model (top) and with the $k-\omega$ SST (bottom).

turbulence and heat transfer near wall and shear-free boundaries, International journal of heat and fluid flow **21**, 37 (2000).

[21] P. Wikström, S. Wallin, and A. V. Johansson, Derivation and investigation of a new explicit algebraic model for the passive scalar flux, Physics of fluids **12**, 688 (2000).

[22] S. Manservisi and F. Menghini, A CFD four parameter heat transfer turbulence model for engineering applications in heavy liquid metals, International Journal of Heat and Mass Transfer **69**, 312 (2014).

[23] S. Manservisi and F. Menghini, CFD simulations in heavy liquid metal flows for square lattice bare rod bundle geometries with a four parameter heat transfer turbulence model, Nuclear Engineering and Design **295**, 251 (2015).

[24] A. Shams and A. De Santis, Towards the accurate prediction of the turbulent flow and heat transfer in low-prandtl fluids, International Journal of Heat and Mass Transfer **130**, 290 (2019).

[25] W. M. Kays, Turbulent Prandtl number. Where are we?, ASME Transactions Journal of Heat Transfer **116**, 284 (1994).

[26] R. Manceau and K. Hanjalić, Elliptic blending model: A new near-wall Reynolds-stress turbulence closure, Physics of Fluids **14**, 744 (2002).

[27] H. Kawamura, H. Abe, and K. Shingai, DNS of turbulence and heat transport in a channel flow with different Reynolds and Prandtl numbers and boundary conditions, Turbulence, Heat and Mass Transfer **3**, 15 (2000).

[28] I. Tiselj, R. Bergant, B. Mavko, I. Bajsic, and G. Hetsroni, DNS of turbulent heat transfer in channel flow with heat conduction in the solid wall, J. Heat Transfer **123**, 849 (2001).

[29] J. Oder, A. Shams, L. Cizelj, and I. Tiselj, Direct numerical simulation of low-Prandtl fluid flow over a confined backward facing step, International Journal of Heat and Mass Transfer **142**, 118436 (2019).

[30] M. Duponcheel and Y. Bartosiewicz, Direct numerical simulation of turbulent heat transfer at low prandtl numbers in planar impinging jets, International Journal of Heat and Mass Transfer **173**, 121179 (2021).

[31] OpenFOAM v6, `https://www.openfoam.com/releases/openfoam-v6`, accessed: 2023-05-30.

[32] M. Duponcheel, L. Bricteux, M. Manconi, G. Winckelmans, and Y. Bartosiewicz, Assessment of RANS and improved near-wall modeling for forced convection at low Prandtl numbers based on LES up to Re_τ= 2000, International Journal of Heat and Mass Transfer **75**, 470 (2014).

[33] S. Banerjee, R. Krahl, F. Durst, and C. Zenger, Presentation of anisotropy properties of turbulence, invariants versus eigenvalue approaches, Journal of Turbulence , N32 (2007).

[34] C. M. Bishop, Pattern recognition and machine learning, Springer google schola **2**, 1122 (2006).

[35] S. M. Lundberg and S.-I. Lee, A unified approach to interpreting model predictions, Advances in neural information processing systems **30** (2017).

[36] M. Sundararajan, A. Taly, and Q. Yan, Axiomatic attribution for

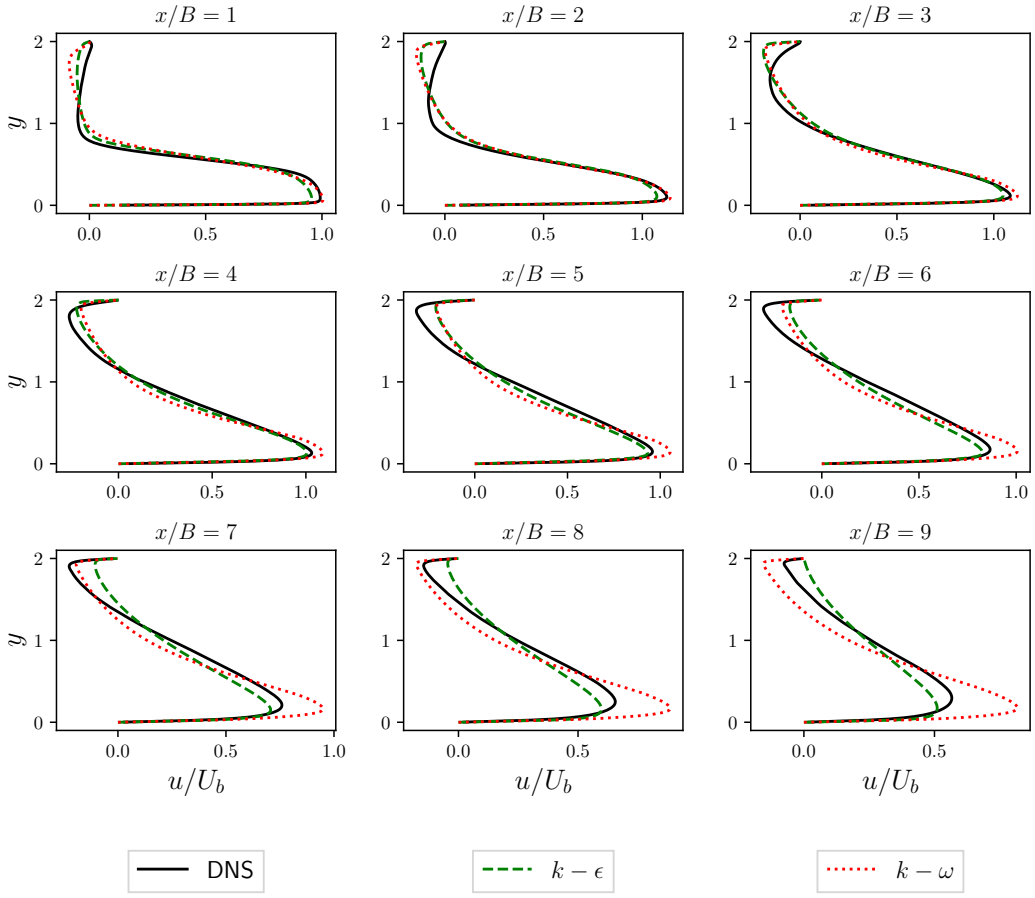

FIG. 24: Streamwise velocity profiles computed with different RANS momentum treatments at several distances from the impinging point ($x/B = 0$). Comparison with the reference DNS data [30].

deep networks, arXiv preprint arXiv:1703.01365 (2017).

[37] R. Maulik, H. Sharma, S. Patel, B. Lusch, and E. Jennings, Deploying deep learning in openfoam with tensorflow, in *AIAA Scitech 2021 Forum* (2021) p. 1485.

[38] M. Fiore, *Thermal Turbulence Modeling of Heavy Liquid Metals via Data Analysis and Machine Learning*, Ph.D. thesis, Université catholique de Louvain, Louvain-la-Neuve, Belgium (2023).

[39] G. Grötzbach, Challenges in low-prandtl number heat transfer simulation and modelling, Nuclear engineering and design **264**, 41 (2013).

[40] Note that the sign of the coefficients a_i does not alter the final output, since $\mathbf{A} = \sum a_i \mathbf{T}^i$ is the Cholesky factorization of the symmetric part of $\mathbf{D}$, as indicated by eq.(6).

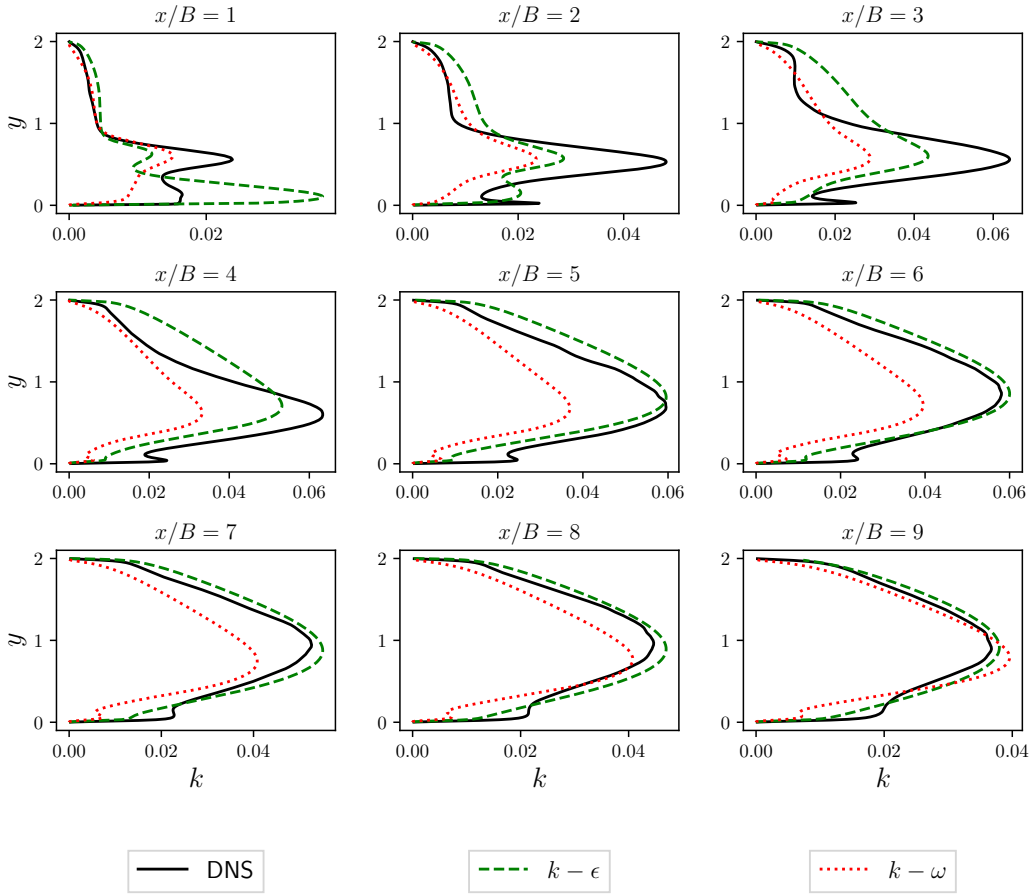

FIG. 25: Profiles of the turbulent kinetic energy computed with different RANS momentum treatments at several distances from the impinging point ($x/B = 0$). Comparison with the reference DNS data [30].

TABLE VI: Overview of the boundary conditions imposed for the RANS simulation of turbulent channel flows.

Field	Inlet	Outlet	Walls
$\mathbf{U}$	Cyclic	Cyclic	$\mathbf{U} = 0$
p	Cyclic	Cyclic	$\frac{\partial p}{\partial n} = 0$
k	Cyclic	Cyclic	$k = 0$
ε	Cyclic	Cyclic	$\varepsilon = 0$
$\overline{\mathbf{uu}}$	Cyclic	Cyclic	$\overline{\mathbf{uu}} = 0$

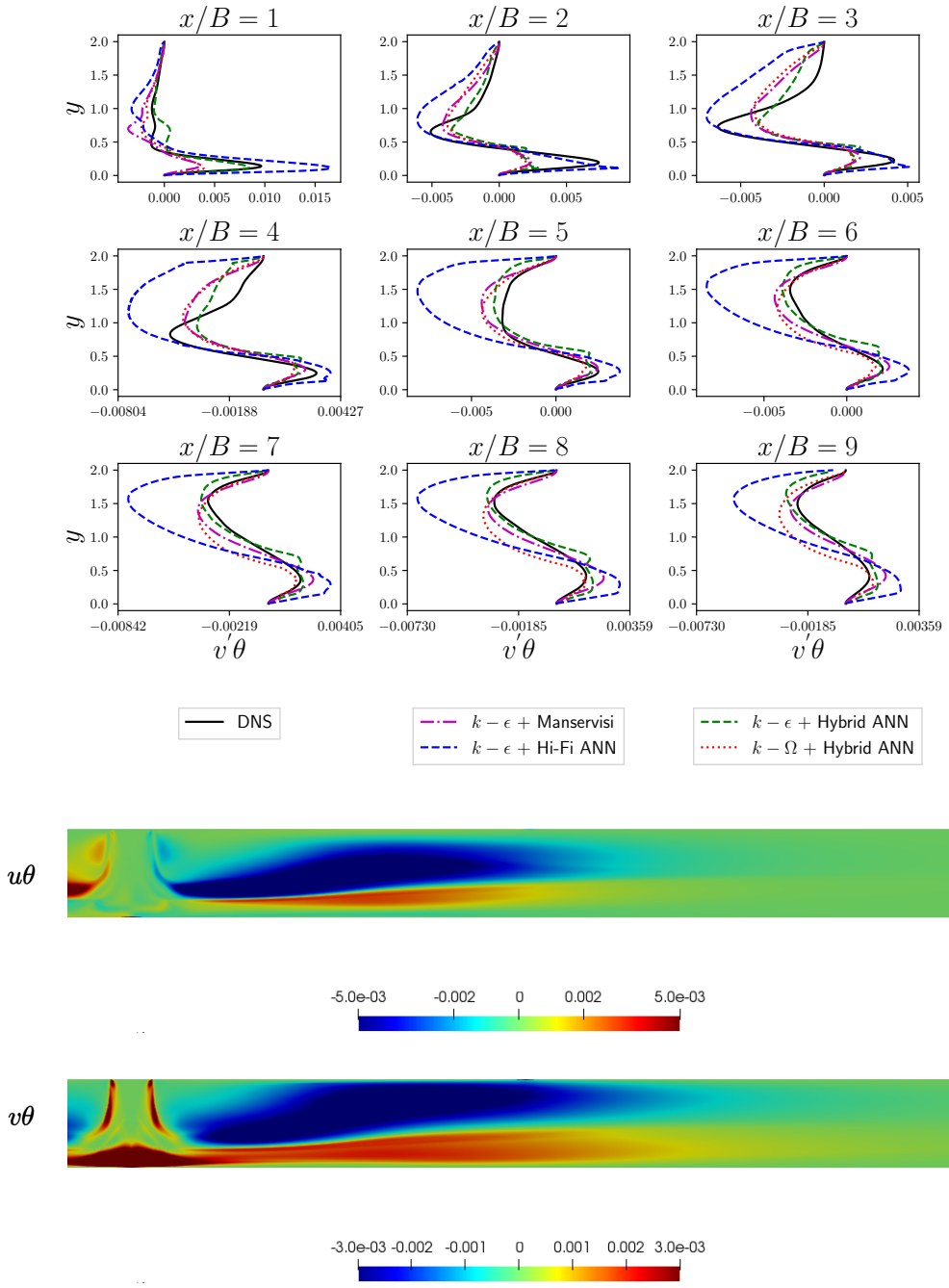

FIG. 26: Top: wall normal heat flux profiles obtained with the hybrid ANN, the Hi-Fi ANN and Manservisi model [22]. Comparison with the DNS data [30] at several distances from the impinging point. Bottom: contours of the streamwise ($\overline{u\theta}$) and wall normal ($\overline{v\theta}$) heat fluxes.

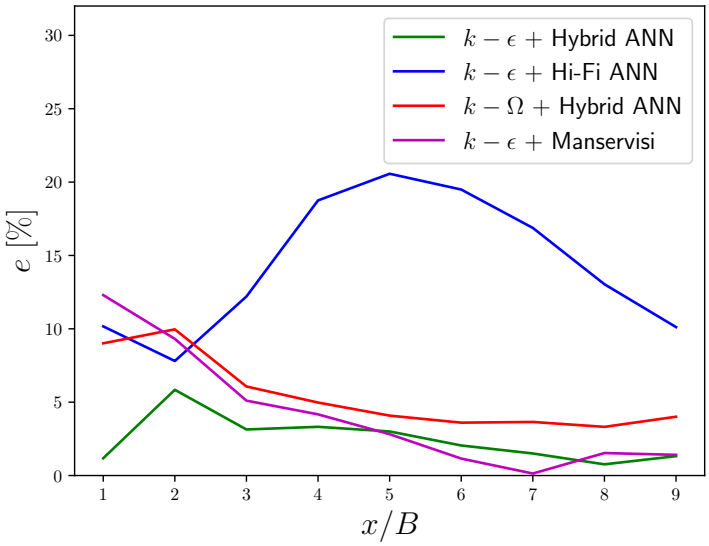

FIG. 27: Average percentage error in the wall-normal turbulent heat flux computed with different momentum and thermal turbulence closures.

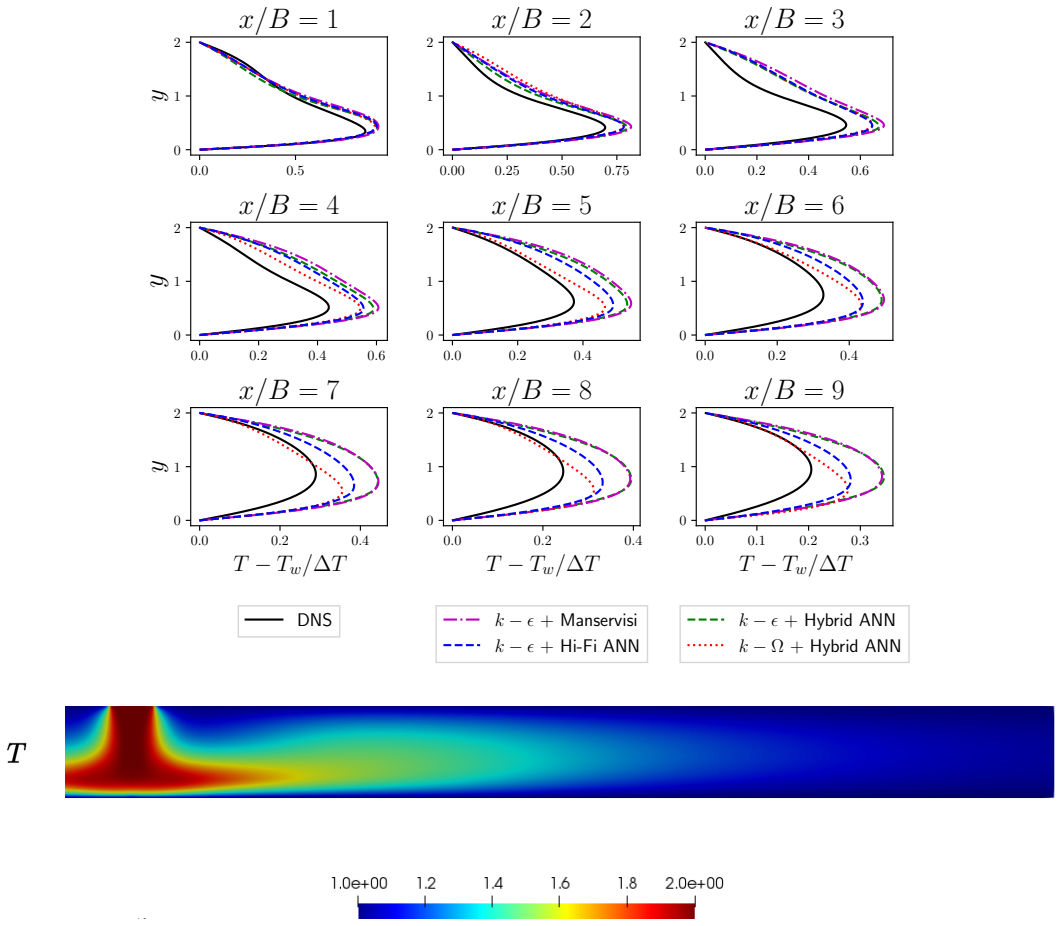

FIG. 28: Top: temperature profiles obtained with the hybrid ANN, the Hi-Fi ANN and the Manservisi model [22]. Comparison with the DNS data [30] at several distances from the impinging point. Bottom: contour of the temperature field.

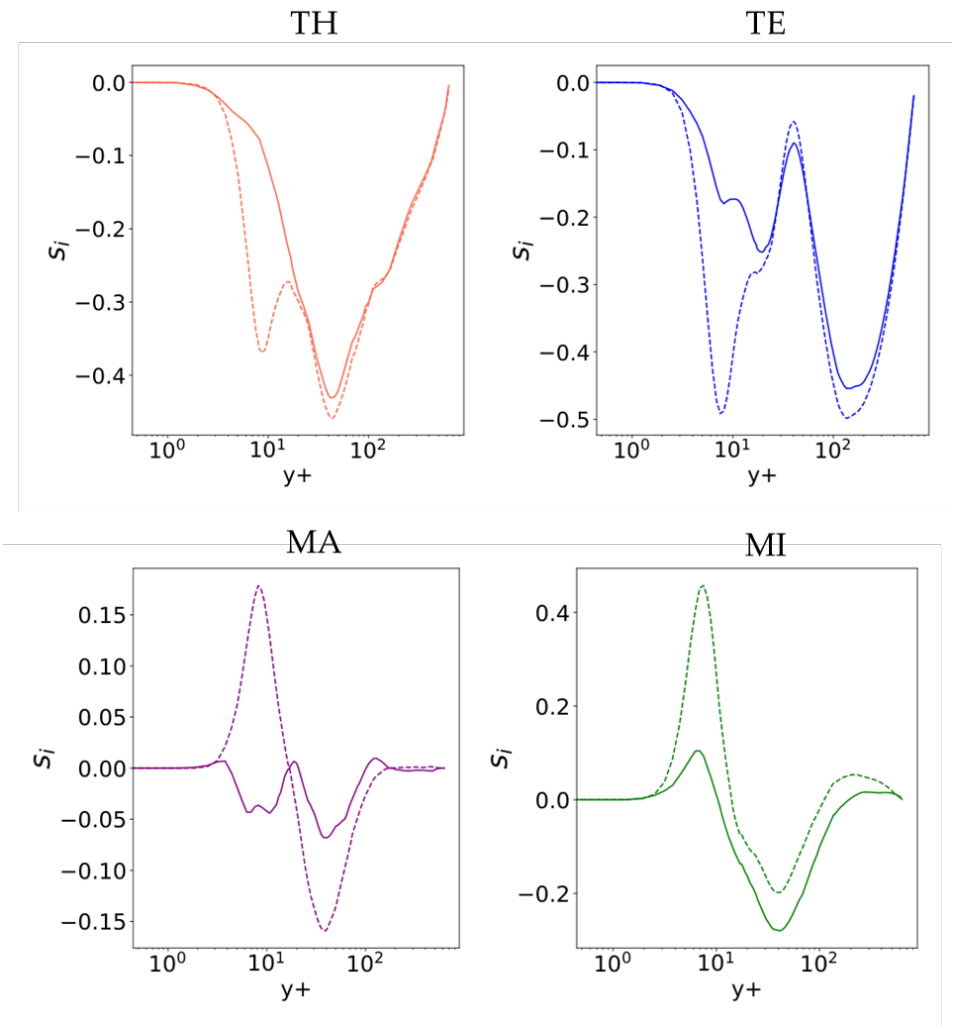

FIG. 29: Comparison between the Shapley values obtained for the Hi-Fi network (dashed line) and hybrid network (solid line) for the wall-normal component of the heat flux at $Pr = 0.71$.